8-2021

Fabrication and Characterization of Polyvinylidene Fluoride Nanofibers for Energy Harvesting Applications

Jui Vitthal Kharade
The University of Texas Rio Grande Valley

FABRICATION AND CHARACTERIZATION OF POLYVINYLIDENE FLUORIDE NANOFIBERS FOR ENERGY HARVESTING APPLICATIONS

A Thesis

by

JUI VITTHAL KHARADE

Submitted to the Graduate College of
The University of Texas Rio Grande Valley
In partial fulfilment of the requirements for the degree of

MASTER OF SCIENCE IN ENGINEERING

August 2021

Major Subject: Mechanical Engineering

CHARACTERIZATION AND FABRICATION OF POLYVINYLIDENE FLUORIDE NANOFIBERS FOR ENERGY HARVESTING APPLICATION

A Thesis
by
JUI VITTHAL KHARADE

COMMITTEE MEMBERS

Dr. Horacio Vasquez
Chair of committee

Dr. Karen Lozano
Committee Member

Dr. Mataz Alcoutlabi
Committee Member

August 2021

ABSTRACT

Kharade, Jui Vitthal, Fabrication and Characterization of Polyvinylidene Fluoride Nanofibers for Energy Harvesting Applications. Master of Science in Engineering (MSE), August, 2021, 89 pp. 4 table, 57 figures, references, 67 titles

Miniaturization of portable devices demand a power source that does not require recharging from the grid or replacement; instead, it requires a self-charging or self-powering mechanism. Piezoelectric energy harvesters are devices that harvest mechanical energy from the environment and convert it into electrical energy and are good candidates to power and/or recharge those devices. The main objective of this thesis is to fabricate piezoelectric fiber mats to be used as an energy harvester to charge capacitors or batteries.

In this thesis, the effect of fabricating procedures, solvents, and composites on polyvinylidene nanofibers are analysed in order to improve the piezoelectric response of nanofiber mats. These nanofiber mats are then used for fabricating an energy harvester to charge capacitors. A vibrating machine was created to test the response of nanofiber mats to vibrations at adjustable magnitude and frequency of oscillation and to charge a capacitor using these vibrations. The charging circuit and the results obtained are also presented in this thesis.

DEDICATION

This study is dedicated to my family. This project would not have been possible without their love and support. Thank you for supporting me.

ACKNOWLEDGMENT

I would like to express my gratitude to Dr. Horacio Vasquez, my thesis committee chair, for his support, advice and for giving me the opportunity to work on this project. I am thankful towards my thesis committee members: Dr. Karen Lozano and Dr. Mataz Alcoutlabi for their support, input, advice and for resources. I would like to thank Dr. M. Jasim Uddin, Dr. Mircea Chipara and Dr. Javier Macossay-Torres for providing resources and insight to ensure completion and quality of this project. I would like to thank Dr. Victoria Padilla for providing resources and ensuring a good working environment. I would also like to thank our PREM team at UTRGV for their support and insights.

TABLE OF CONTENTS

Page

LIST OF TABLES

Page

LIST OF FIGURES

Page

CHAPTER I

INTRODUCTION

1.1 Statement of Problem

With miniaturization of portable and wireless devices, power sources without the need for recharging or replacement are in demand (Safaei et al., 2019). Conventional batteries have multiple disadvantages such as limited life span, limited capacity, need for recharging or replacement and toxicity (Safaei et al., 2019 & Sathya, 2020). A promising solution for these problems is energy harvesters. Energy harvesters are devices that harness energy from ambient environment and convert it to electrical energy. Ideal energy harvesters are not required to be recharged or replaced; therefore, energy harvesters are good replacements for batteries or battery chargers connected to the grid. One of the methods for harvesting energy from environment is with piezoelectric materials which can overcome the disadvantages of batteries. Therefore, in this research, a piezoelectric energy harvester was fabricated using nanofiber mats, and it was characterized and tested in a capacitor charging circuit.

1.2 Statement of Purpose

This research project focuses on the characterization of piezoelectric nanofibers and fabrication and testing of a piezoelectric energy harvester to harness energy from ambient mechanical energy. Polyvinylidene fluoride (PVDF) is selected as the piezoelectric material due to its non-toxic, biocompatible, flexible nature and ease of fabrication as nanofiber mats. The objectives of this research project are:

1. Test the effect of different nanoparticles (multiwalled carbon nanotubes and barium titanate) and fabrication processes on the piezoelectricity and morphology of polyvinylidene fluoride nanofiber mats using Fourier transform infrared spectroscopy and scanning electron microscopy.
2. Testing the output voltage response of the nanofiber mats to applied stress using a pneumatic press and an oscilloscope.
3. Fabricating an energy harvester and testing it using a vibrating machine assembled in house for charging a capacitor using an electric circuit that includes a rectifier.

1.3 Piezoelectricity

Piezoelectricity is named after the Greek word ‘piezein’ which means to press or squeeze. In 1880, brothers Pierre and Jacques Curie demonstrated the direct piezoelectric effect for the first time (Ballato, 1995; Swallow et al., 2008; and Vijaya, 2013). There are two types of piezoelectric effects: direct and indirect piezoelectric. Direct piezoelectric effect is the property of a material to produce an electric field when the material is subjected to deformation or mechanical stress. The property of the material to deform when subjected to an electric field is called the indirect piezoelectric effect. Pierre and Jacques Curie did not predict the indirect piezoelectric effect.

Instead, Gabriel Lippmann predicted the existence of the indirect piezoelectric effect and the Curie brothers then confirmed it. Figure 1 and Figure 2 show the illustrations of direct and indirect piezoelectric effects, respectively.

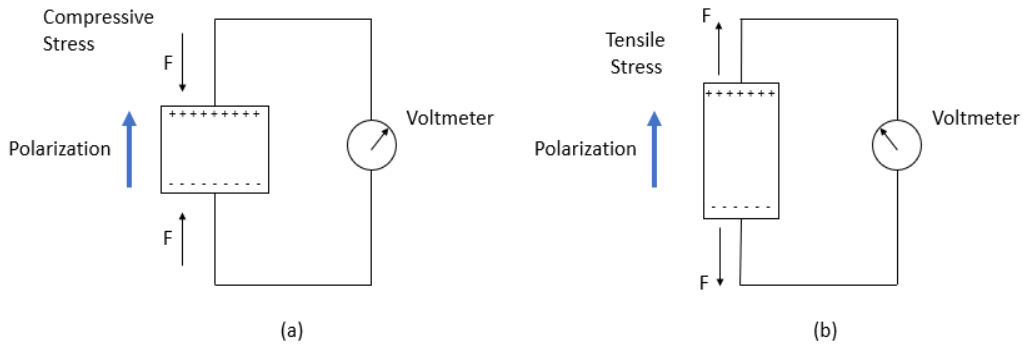

Figure 1: Direct piezoelectric effect- Mechanical strain produces electric voltage

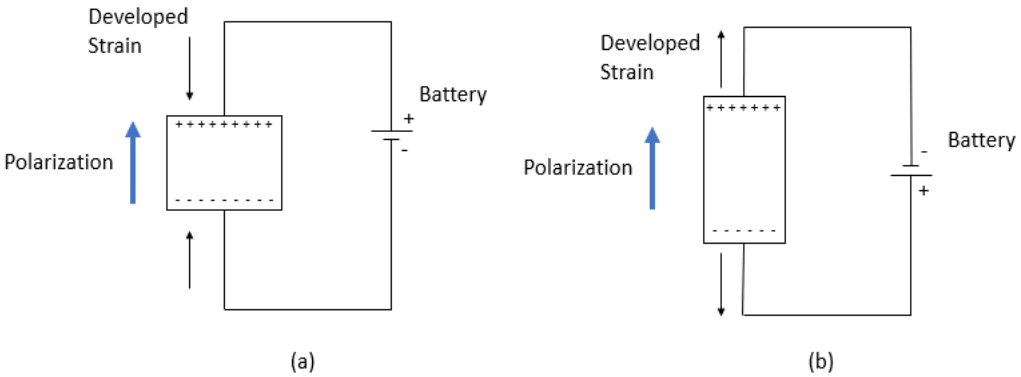

Figure 2: Indirect piezoelectric effect- Electric voltage produces mechanical deformation

Pyroelectricity and ferroelectricity are two important properties associated with piezoelectricity. Pyroelectric materials possess the ability of producing an electric field with changes in temperature, and the corresponding property is called pyroelectricity. All pyroelectric materials are piezoelectric, but not all piezoelectric materials are pyroelectric. Ferroelectric materials possess a permanent electric dipole moment, and the corresponding property is called

ferroelectricity (Ballato, 1995). A material can only be ferroelectric if it is pyroelectric. All pyroelectric and ferroelectric materials are piezoelectric, but the converse is not necessarily true (Vijaya, 2013). Figure 3 shows the classification of dielectric materials. Figure 4 shows the relationship between electrical, mechanical, and thermal properties for dielectric materials.

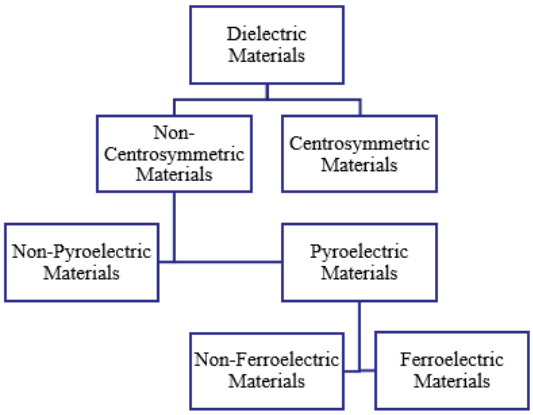

Figure 3: Classification of Dielectric Materials

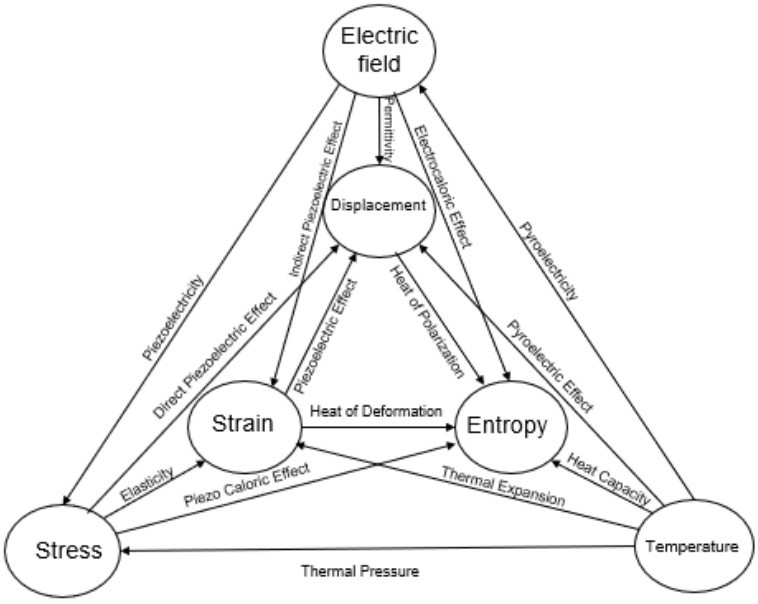

Figure 4: Relationships between electrical, mechanical, and thermal properties.

It was not until 1917 that the first practical application of piezoelectricity was developed. Paul Langevin developed an ultrasonic submarine detector during world-war 1 (Mould, 2007). Piezoelectricity is observed in materials with non-centrosymmetric crystal structure. Non-centrosymmetric materials are the materials in which the unit cells do not possess a centre of symmetry i.e., the molecule does not possess a centre of inversion. Inversion centre is a point about which the reflection of a component yields the component to superimpose on itself. These non-centrosymmetric molecules possess a dipole moment which consists of a partial positive charge on one side and a partial negative charge on another side. The basic reason for occurrence of these dipole moments is electronegativity.

Electronegativity is the ability of an atom to attract electrons in a covalent bond towards itself. Different atoms have a different electronegativity. Out of all the elements in the periodic table, fluorine is the most electronegative with an electronegativity of four. When two atoms with different electronegativity share a covalent bond, the atom with highest electronegativity tends to attract the electrons in the bond towards itself. Therefore, the electrons shift towards the atom with high electronegativity. This causes the high electronegative atom to acquire a partial negative charge and the low electronegative atom to acquire a partial positive charge. This creates a dipole moment in the direction of the highly electronegative atom.

Figure 5 shows a carbon atom and a fluorine atom with a covalent bond between them. As electronegativity of the fluorine atom is higher than the carbon atom, the electrons in the covalent bond are slightly more attracted to the fluorine atom. This creates a partial negative charge on the fluorine atom and a partial positive charge on the carbon atom. These charges create a dipole moment. The direction of the dipole charge is as shown in figure. When there are more than two

atoms in a molecule, the magnitude and the direction of the dipole moment depends on the net partial positive and negative charges.

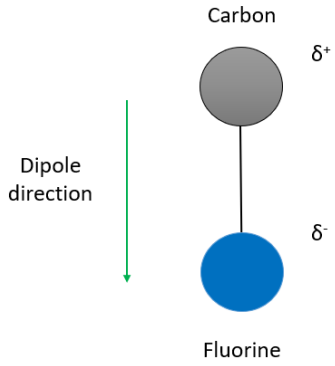

Figure 5: Dipole moment between carbon and fluorine

In centrosymmetric materials, since the molecules have a point of symmetry, the cumulative dipole moment of the molecule is zero. Since the non-centrosymmetric materials are not arranged in a symmetric order, the net dipole moment of the molecule is not zero. Although the molecules possess a dipole moment, since the molecules are randomly arranged in different directions, their dipoles usually cancel each other, and the material as a whole does not possess a dipole moment. When pressure is applied on the piezoelectric material, the structure of atoms in the material is disturbed and the net dipole moment becomes non-zero, causing the material to acquire a positive charge on one face and negative charge on another resulting in an electric voltage. For a piezoelectric material, the constituent equations are given by (Sirohi & Chopra, 2000):

$$D_i = e_{ij}^{\sigma} E_j + d_{im}^{d} \sigma_m \quad (1)$$

$$\varepsilon_k = d_{jk}^{c} E_j + s_{km}^{E} \sigma_m \quad (2)$$

Here, D_i is the electric displacement in C/m^2 with size (3 x 1), E_j is the electric field vector in V/m with size (6 x 1), σ_m is the stress vector in N/m^2 with size (6 x 1), ε is the strain vector with size (6 x 1), $e_{ij}^{\sigma}$is the dielectric permittivity in F/m with size (3 x 3), $d_{im}^{d}$is the piezoelectric coefficient in C/N with size (3 x 6), $d_{jk}^{c}$is the piezoelectric coefficient in m/V with size (6 x 3), and s_{km}^{E} is the elastic compliance in m^2/N with size (6 x 6). The superscript c and d correspond to converse and direct piezoelectric effects, respectively. The superscript σ indicates that the value measured is at constant stress and the superscript E indicates that the value measured is at constant electric field (Sirohi & Chopra, 2000). For a piezoelectric film, the coordinate system is given in Figure 6.

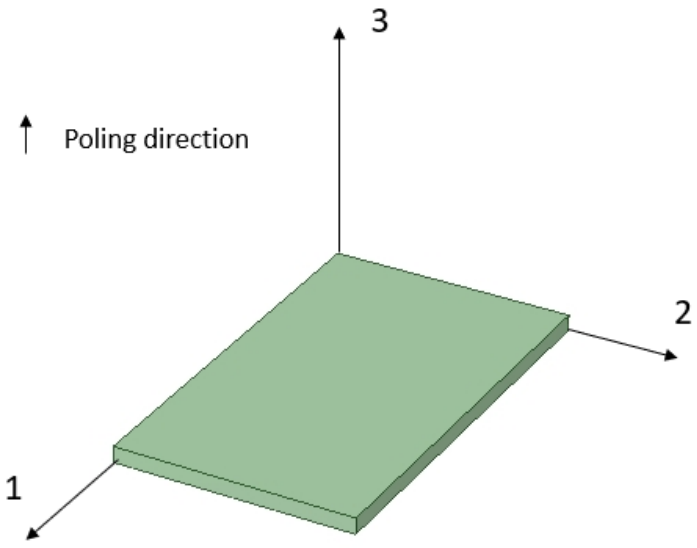

Figure 6: Coordinate system for piezoelectric film

For piezoelectric films, the constituent equations (1) and (2) can be written in matrix form as (Sirohi & Chopra, 2000):

$$\begin{bmatrix} D_1 \\ D_2 \\ D_3 \end{bmatrix} = \begin{bmatrix} e_{11}^{\sigma} & 0 & 0 \\ 0 & e_{22}^{\sigma} & 0 \\ 0 & 0 & e_{33}^{\sigma} \end{bmatrix} \begin{bmatrix} E_1 \\ E_2 \\ E_3 \end{bmatrix} + \begin{bmatrix} 0 & 0 & 0 & 0 & d_{15} & 0 \\ 0 & 0 & 0 & d_{24} & 0 & 0 \\ d_{31} & d_{32} & d_{33} & 0 & 0 & 0 \end{bmatrix} \begin{bmatrix} \sigma_1 \\ \sigma_2 \\ \sigma_3 \\ \sigma_4 \\ \sigma_5 \\ \sigma_6 \end{bmatrix} \tag{3}$$

$$\begin{bmatrix} \varepsilon_1 \\ \varepsilon_2 \\ \varepsilon_3 \\ \varepsilon_4 \\ \varepsilon_5 \\ \varepsilon_6 \end{bmatrix} = \begin{bmatrix} 0 & 0 & d_{31} \\ 0 & 0 & d_{32} \\ 0 & 0 & d_{33} \\ 0 & d_{24} & 0 \\ d_{15} & 0 & 0 \\ 0 & 0 & 0 \end{bmatrix} \begin{bmatrix} E_1 \\ E_2 \\ E_3 \end{bmatrix} + \begin{bmatrix} S_{11} & S_{12} & S_{13} & 0 & 0 & 0 \\ S_{21} & S_{22} & S_{23} & 0 & 0 & 0 \\ S_{31} & S_{32} & S_{33} & 0 & 0 & 0 \\ 0 & 0 & 0 & S_{44} & 0 & 0 \\ 0 & 0 & 0 & 0 & S_{55} & 0 \\ 0 & 0 & 0 & 0 & 0 & S_{66} \end{bmatrix} \begin{bmatrix} \sigma_1 \\ \sigma_2 \\ \sigma_3 \\ \sigma_4 \\ \sigma_5 \\ \sigma_6 \end{bmatrix} \tag{4}$$

These equations are for an actuator which is based on indirect or converse piezoelectric effect. A sensor or an energy harvester is based on the direct piezoelectric effect. Therefore, the equation for a sensor can be given by (Sirohi & Chopra, 2000):

$$\begin{bmatrix} D_1 \\ D_2 \\ D_3 \end{bmatrix} = \begin{bmatrix} 0 & 0 & 0 & 0 & d_{15} & 0 \\ 0 & 0 & 0 & d_{24} & 0 & 0 \\ d_{31} & d_{32} & d_{33} & 0 & 0 & 0 \end{bmatrix} \begin{bmatrix} \sigma_1 \\ \sigma_2 \\ \sigma_3 \\ \sigma_4 \\ \sigma_5 \\ \sigma_6 \end{bmatrix} \tag{5}$$

In this thesis, the voltage across direction 3 is measured in the nanofiber mats. Therefore, the equation will be:

$$D_3 = d_{31}\sigma_1 + d_{32}\sigma_2 + d_{33}\sigma_3$$

In this equation, D_3 is the electric displacement in direction 3 of the nanofiber mat shown in Figure 6. d_{31}, d_{32}, and d_{33} are the piezoelectric coefficients and σ_1, σ_2, and σ_3 are the stresses applied in directions 1, 2 and 3 respectively.

1.4 Piezoelectric materials

There are numerous natural and synthetic piezoelectric materials available. Basic classification of piezoelectric materials is shown in Figure 7. Piezoelectric materials can be classified in four categories. Some of the naturally occurring piezoelectric crystals are quartz, sucrose, rochelle salt, topaz, tourmaline, berlinite. tendon, silk, dentin, enamel, and collagen are some of the biological piezoelectric materials. barium titanate, lead zirconate titanate, lead titanate, sodium tungstate and sodium niobate are some of the piezoelectric ceramics. Polyvinylidene fluoride, polyamides and polyurethanes are some of the piezoelectric polymers.

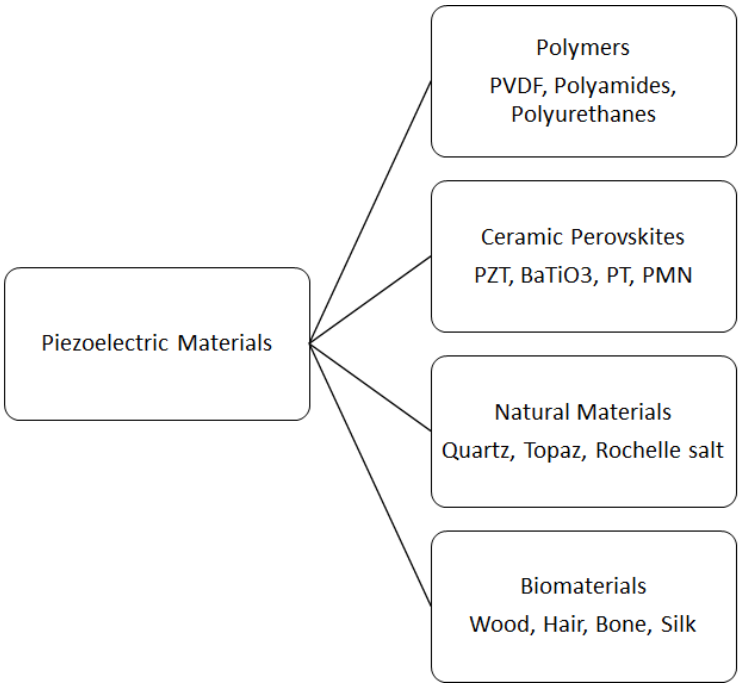

Figure 7: Classification of piezoelectric materials

.

In 1950s, Bazhenov observed the piezoelectric effect in wood for the first time. Later in 1955, Fukada verified the converse piezoelectric effect of wood (Fukada, 1968 & 2000). In 1957 and 1964, Yasuda and Fakuda observed piezoelectric properties in ordered native collagen (Fukada, 1968, 2000 and Kaczmarek, 2019). Collagen is present in bones, skin, connective tissues, and tendons. More and Kapusetti (2017) presented a hypothesis where a piezoelectric scaffold could be used for tissue regeneration. The piezoelectric scaffold placed at the damage site will be subjected to functionalized loads and will generate an electric voltage. This potential difference could stimulate the nearby tissues and bones using their natural piezoelectric properties thus promoting tissue regeneration and bone remodelling. Maiti et al. (2017) proved that onion skin can be an efficient bio compatible energy harvester. Research has shown that biowaste eggshell membrane has a good source of collagen; therefore, eggshell membranes possess piezoelectricity. A nanogenerator similar to onion skin nanogenerator can be fabricated using eggshell membranes (Kaczmarek, 2019). A self-powered and durable onion skin biocompatible nanogenerator was fabricated (Kawai, 1969) observed piezoelectricity in polarized polyvinyl fluoride, polyvinyl chloride, polycarbonate, polyethylene, and polytetrafluoroethylene (Kawai, 1969).

Lead zirconate titanate or PZT (ceramic) is one of the most widely used piezoelectric materials. Though the energy efficiency of PZT is high, it is extremely brittle and therefore, cannot be used for applications requiring high strain (Anton & Sodano, 2017). Toxic lead contents of PZT devices makes them unsuitable for many applications requiring biocompatibility (Akin et al., 2018). Polyvinylidene fluoride is one of the most commonly used piezoelectric polymer. Table 1 shows the properties of some common piezoelectric materials. Although, the piezoelectric coefficient of PVDF is less than PZT, it is flexible, biocompatible nontoxic since it does not contain

lead. Therefore, PVDF is an ideal candidate for energy harvesters, especially in biomedical applications.

Table 1: Properties of piezoelectric materials (Elahi et al., 2018)

Material	d_{31} x10^{-12} (m/V)	d_{33} x10^{-12} (m/V)	d_{15} x10^{-12} (m/V)
Polyvinylidene fluoride	18-24	-33	-
Lead zirconate titanate	-274	593	741
Barium titanate	-33	82	150
Potassium-sodium niobate	-	689	-

1.4.1 Polyvinylidene Fluoride.

One of the widely used piezoelectric polymers is polyvinylidene fluoride (PVDF) with the molecular formula $C_2H_2F_2$. Figure 8 shows the PVDF monomer.

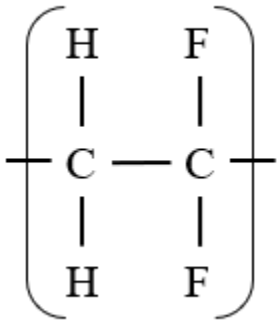

Figure 8: Polyvinylidene fluoride monomer

PVDF is a semicrystalline polymer containing about 50 -54 % crystalline phase and the rest is amorphous (Broadhurst & Davis, 1884; Sencadas et al., 2009; and Tiwari & Srivastava, 2014).

In 1969, Kawai observed that PVDF films exhibit piezoelectric behaviour after they have been stretched at a temperature of 100-150 ^{o}C and subjected to a high voltage electric field. PVDF is flexible and can achieve high piezoelectric properties when properly fabricated. Based on the chain conformation, PVDF possess five phases namely α, β, γ, δ and ε. The α-phase has a trans-gauche twist chain conformation (TGTG'). The α and ε are non-polar phases while β, γ and δ are the polar phases. β-phase having all trans planar zigzag chain conformation (TTTT) is the most polar and therefore widely used in piezoelectric applications (Martins et al., 2014). The γ-phase is an intermediate conformation between the α and β phases (TTTGTTTG'). The δ phase has the same chain conformation as α-phase but a different packing structure. Figure 9 shows the

molecules of the phases of PVDF. It can be inferred from Figure 9 that the net dipole moment in a α phase molecule is zero since, the alternating arrangement of fluorine atoms cancels out the dipole moments.

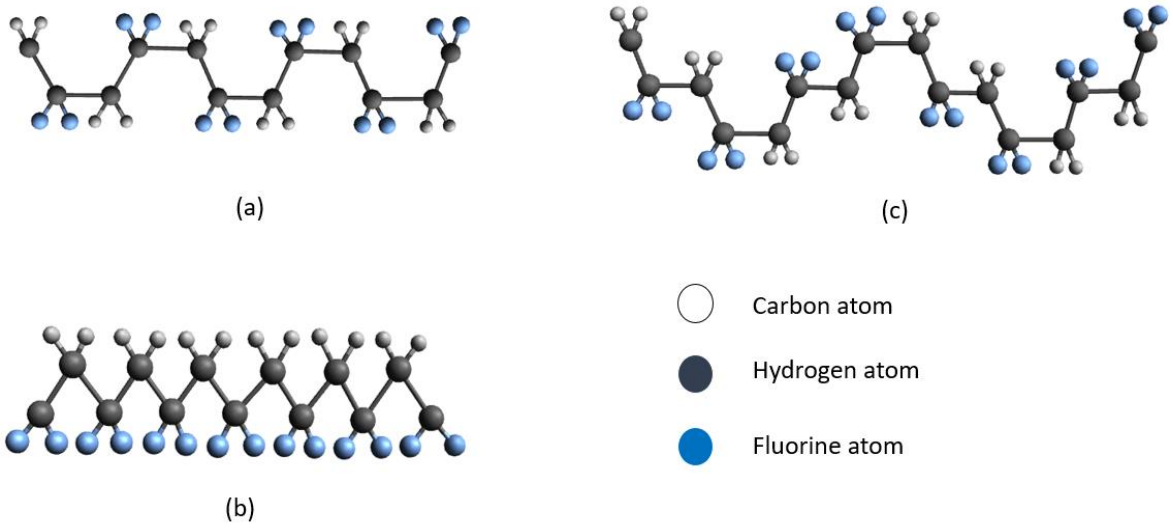

Figure 9: Phases of PVDF (a) α-phase, (b) β-phase and (c) γ-phase

The potential energy of the β-phase is -5.73 kcal/mol and that of α-phase is -6.03 kcal/mol (Nishiyama et al., 2016). Therefore the α-phase is the most stable phase. Therefore, α phase is formed from melt. The β-phase can be obtained from the most stable α-phase by application of high temperature and high electric fields. Solution casting, stretching, poling, and hot compression are some of the techniques used to convert α-phase to β-phase. The range of electrical dipole moment of the PVDF monomer unit for different phases is 5×10^{-30} C·m to 8×10^{-30} C·m. Unlike some conventional ceramic materials, PVDF is flexible, biocompatible, easy to handle and possesses high mechanical strength. Figure 11 shows the β-phase molecule of PVDF. As the net partial charges are not balanced, there is a higher dipole moment. The direction of the dipole moment is as shown in Figure 10.

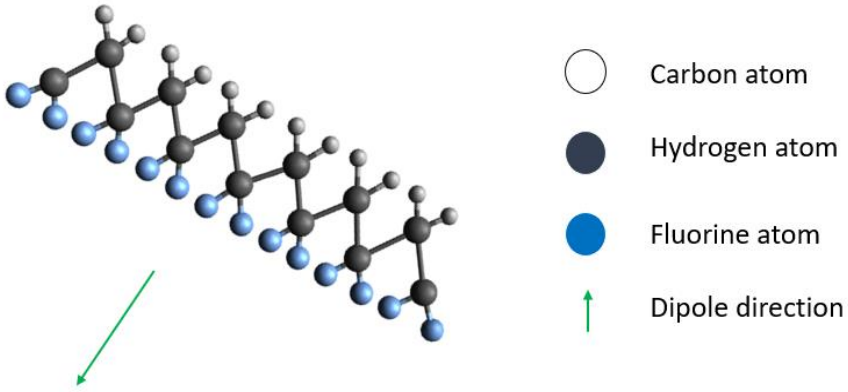

Figure 10: Dipole moment of β-phase of PVDF

1.4.2 Polyvinylidene Fluoride Composites.

Composites are used in order to improve certain properties of a material. It has been known that the piezoelectric properties of PVDF depend on the amount of β-phase in the structure. Commonly used methods to increase β-phase are stretching and poling. Apart from these, addition of certain nanoparticles to PVDF have shown to increase the β-phase significantly. Research shows that carbon nanotubes or barium titanate ($BaTiO_3$ / BTO) composite with PVDF would be able to increase the β phase in PVDF significantly.

1.4.2.1 Barium Titanate/PVDF Composite. Barium Titanate ($BaTiO_3$/BTO) is a piezoelectric material that belongs to the perovskite material family with a general formula ABO_3. Similar to PVDF, BTO exhibits multiple phases. BTO has 4 phases: cubic phase, tetragonal phase, rhombohedral phase, and orthogonal phase. Out of these, except the cubic phase, all phases are ferroelectric (Acosta et al., 2017). BTO exhibits good piezoelectric properties, excellent mechanical properties, and low cost. Research has shown that addition of BTO to PVDF might be able to increase the β-phase and thus piezoelectricity. Also, as BTO is piezoelectric itself and exhibits a higher piezoelectric coefficient than PVDF, it may increase the piezoelectric response without increasing the β-phase (Elahi et al., 2018). Singh et al. (2019) characterized PVDF and BTO composite films, the fourier transform infrared spectra (FTIR) and X-ray diffraction (XRD) spectra clearly indicated an increase in β-phase of PVDF. Yang et al. (2020) fabricated a flexible piezoelectric pressure sensor using polydopamine modified BTO and PVDF composite film. Aluminium was used as electrodes. The sensor was poled at 50 MV/m. With 12 N force, the sensor was able to produce a voltage of 9.3 V. This result was 13.3 times higher than PVDF alone which produced a voltage of 0.7 V. Shuai et al. (2020) fabricated a scaffold with polydopamine functionalized BTO and PVDF. The β-phase fraction of PVDF was increased by 11%. The open circuit voltage increased from 1.8 V for PVDF to 7 V for 1% BTO. The short circuit current increased from 18 nA to 90.4 nA. Zhao et al. (2015) tested the response of PVDF film with BTO. They observed an increase in output voltage from 15 V for PVDF film to 35 V to composite film under 1 MPa pressure (145 psi).

1.4.2.2 Carbon Nanotubes/PVDF Composite. Carbon nanotubes (CNT) are carbon structures in a tubular form with radius in nanometer scale. They have a large length to diameter ratio. Carbon nanotubes can be multiwalled (MWCNT) or single walled (SWCNT) (Popov, 2004). Between SWCNTs and MWCNTs, small diameter MWCNTs exhibit better reinforcement with polymers and thus are a better choice for PVDF composites (Cadek et al., 2004). Research has shown that addition of carbon nanotubes could be able to increase the β-phase in PVDF and thus improve the piezoelectric response. Liu et al. (2013) investigated the properties of PVDF and MWCNTs nanofibers. XRD analysis showed increase in β-phase with addition of MWCNTs. Although it is not possible to obtain β-phase from pure PVDF melt, research shows that it is possible to obtain β-phase from PVDF melt if carbon nanotubes are added to the melt. PVDF films prepared from melt with MWCNTS which are drawn and poled show a very high or almost pure β-phase i.e., up to 96%. Although addition of CNTs increases the PVDF β-phase, there is a critical limit for the amount of CNTs after which the β-phase starts decreasing (Kim et al, 2009). CNTs can improve the sound absorption of PVDF films as well by shifting the absorption spectra to a lower frequency. Addition of CNTs to PVDF/PZT composite can increase the piezoelectric coefficient. It can be implied that, addition of carbon nanotubes to PVDF or PVDF composites is beneficial if the amount of CNT is less than 1 wt %. Mahanty et al. (2020) fabricated a healthcare monitor or e-skin monitor using electrospun PVDF and MWCNT composite; and the e-skin monitor successfully detected the pulses on the wrist and muscle movement on the arm.

1.5 PVDF films

PVDF films can be fabricated using various methods such as spin coating and solution casting. Spin coating consists of a rotating flat disk and the solution of PVDF and dimethyl formamide is deposited on the disk. The rotation of the disk causes the solution to spread out in the form of a film. The solvent is then evaporated at a high temperature. The PVDF film obtained is then peeled from the disk.

In solution casting, the PVDF is dissolved in dimethylformamide (DMF). The solution is then spread out on a petri dish and the solvent is then evaporated by heating it to an appropriate temperature. After that, the PVDF film is peeled from the petri dish. Another method for preparation of PVDF film is hot pressing. In this method, the solution of PVDF and dimethylformamide is pressurized at a high temperature in the form of a film. The solvent is evaporated due to the high temperature and a PVDF film is obtained. The PVDF films obtained from these processes are mostly in the α-phase. Jin et al. (2018) prepared PVDF disks by compressing the PVDF raw material at high pressure(400MPa) and temperature (275^{o}C) in a piston cylinder arrangement. Higher crystallinity and higher melting point were observed in these samples when compared with the samples formed using the solution method. The β-phase obtained was 86.5%. PVDF composite films can also be fabricated for obtaining desired properties. G. H. Kim et al. (2009) fabricated a PVDF and multiwalled carbon nanotube (MWCNT) film. Results showed that the β-phase content increased when the MWCNTs were added up to 0.2 wt.%. M. Cadek et al. (2004) tested the reinforcements of different carbon nanotubes in a polymer matrix and found out that the MWCNT with a small diameter gave better reinforcement than other CNTs.

PVDF films obtained from melt or solution casting mostly contain α-phase. The commonly used technique to induce β-phase in a PVDF film is stretching. Stretching of the films up to

multiple times, 4 to 5 times, its original size rearranges the PVDF molecules thus converting α-phase to piezoelectric β-phase. The stretching is done between 80 ^{o}C and 100 ^{o}C to soften the material. Below 80 ^{o}C, stretching of the films is not possible due to early rupture. The α-phase has a spherulitic structure and at low deformation ratios, after elongation of amorphous tie chains, tilting and slipping of the lamellar crystalline tie chains is observed. Thus, there is an orientation of crystal blocks and further increase in deformation causes the spherulitic structure to transition into microfibrillar structure. This transition can be seen in SEM images shown in Sencadas et al., 2009. Figure 11 shows the schematic diagram of phase transition in PVDF when stretched.

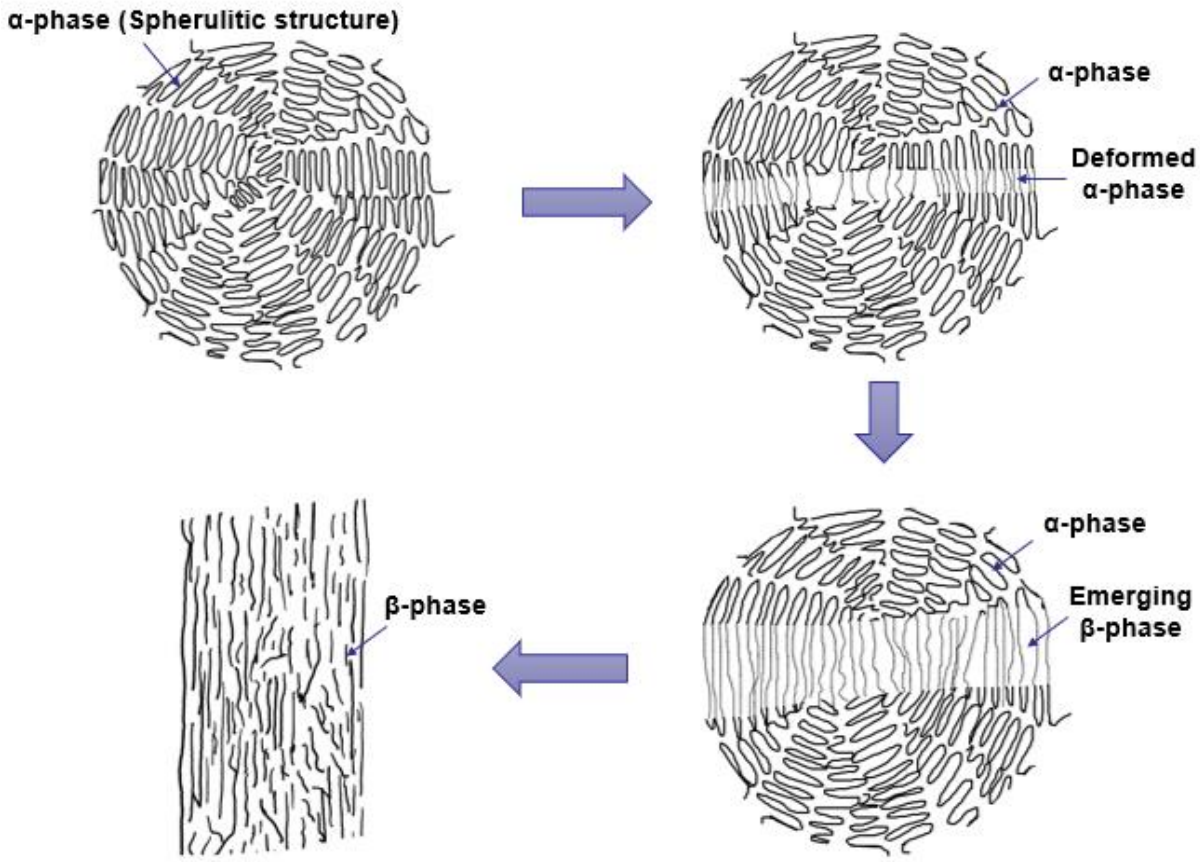

Figure 11: α-phase to β-phase transition schematics for PVDF by stretching.

1.6 PVDF Nanofibers

Nanofibers have diameters in the range of nanometers (1 nm- 100 nm) (Horrocks & Anand, 2000). The most used technique for fabrication of PVDF nanofibers is electrospinning. In addition, forcespinning is a recently developed technique at UTRGV to create fiber mats from solutions. Unlike PVDF films, nanofibers are not required to be stretched since they undergo stretching while fabrication.

1.6.1 Electrospinning.

Electrospinning is a technique which uses high electrostatic forces for production of nanofibers from polymer solutions or melts (Mokhtari et al., 2015). Electrospinning can be stationary collector type or rotating drum type. The setup of electrospinning consists of a syringe with a needle, a syringe pump, a collector, and high voltage positive and negative sources. The collector can be a stationary platform or a rotating drum. A high voltage difference in the order of 30 kV is applied between the needle and the collector. The syringe pump pushes the solution in the syringe through the needle at a specified rate, such as 0.25 ml/hr. Then, the solution accumulates at the tip of the needle due to surface tension. A positive voltage is applied to the needle and a negative voltage is applied to the collector. As the voltage is increased, at a critical value, the electrostatic forces overcome the surface tension resulting in the formation of a Taylor cone. Therefore, a jet of the solution is formed at the end of the Taylor cone towards the collector (Koç et al., 2020). The solution jet between the needle and the collector consists of three regions, the first region is a conical shape called Taylor cone. The second region consists of a stable jet and the third region consists of an unstable solution jet. If the distance between the collector and the

needle is relatively short so that the collector is in the stable jet region, uniform aligned nanofibers can be obtained (Wang et al., 2019).

Figure 12 shows the electrospinning setup used in this project consisting of a syringe filled with the solution and a needle attached to it, as it was custom made for this project. The collector is a rotating cylinder that has adjustable velocity. High voltage electrical connections are applied to the collector and to the needle to form the solution jet. In the actual setup used in this project, the syringe was placed horizontally at one side of the drum, not vertically as shown in Figure 12.

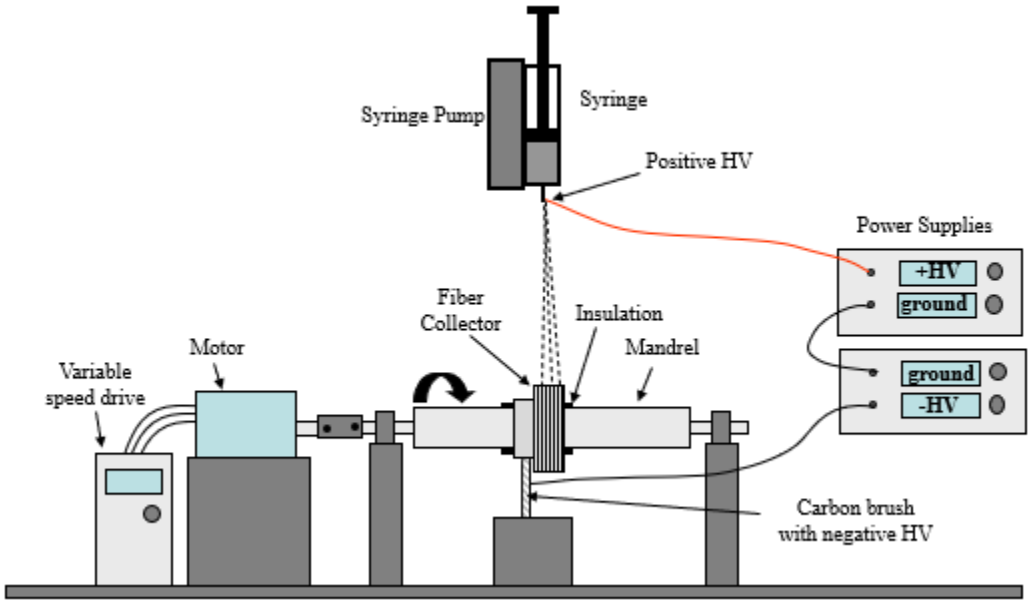

Figure 12: Schematic diagram of electrospinning with rotating collector setup

Important parameters in electrospinning that determine the nanofiber properties are the applied voltage, the flow rate of the solution, distance of the needle tip to the collector and rotating speed of the collector in case of rotating collector electrospinning type. These parameters affect the piezoelectric properties, mechanical properties, morphology, and diameter of the electrospun fiber mat. Low electrospinning voltages are unable to provide the stretching forces that are required for the formation of uniform nanofibers. As discussed, the solution forms a Taylor cone when

subjected to a high electric field. If the voltage is high, a higher flow rate will be required to maintain a stable Taylor cone since a higher voltage will draw more solution through the needle. Properties of the fiber mats also depend on the collector speed significantly, at higher collector speeds and lower flow rates, the fibers may break due to higher forces applied by the collector without enough flow rate (Mokhtari et al., 2016). Formation of β-phase in electrospun PVDF also depends on the amount of stretching the fibers undergo. In stationary electrospinning, since there is no stretching by the collector, the β-phase is expected to be relatively low. Stretching of the jet promotes ordering and formation of all trans configuration, i.e., the β-phase (Mokhtari et al, 2016 and Jiyong et al., 2017). Research shows that fiber diameters decrease with increasing voltage. Although, change in voltage does not affect the β-phase formation significantly. Research conducted by Ribeiro et al. (2010) shows that the amount of β-phase decreases with increase in needle diameter. When the needle diameter was increased from 0.25 mm to 0.50 mm, the β-phase was decreased from 83% to 50 % which is a significant amount (Ribeiro et al., 2010). Typically, there is a decrease in fiber diameter with increase in collector rotating speed. However, after a certain high collector speed, the fiber diameter starts increasing, due to breaking of the fibers as there is excessive stretching of the jet (Motamedi et al., 2017). Diameters of the electrospun nanofibers indicate the amount of stretching the fiber has undergone. Therefore, with increased stretching and decreased diameter, the β-phase in the fibers is expected to be higher.

1.6.2 Forcespinning.

Forcespinning is a recently developed technique for fabricating nanofibers. It was developed by Sarkar et al. (2010) at UTRGV. Forcespinning uses centrifugal force instead of electric field in electrospinning. Unlike electrospinning, both conductive and non-conductive materials can be used in forcespinning. The forcespinning setup consists of a spinneret, a motor to drive the spinneret, a collector to collect the nanofibers, and a controller circuit to control the spinning parameters such as rotating speed, time, and temperature. Figure 13 shows the forcespinning system.

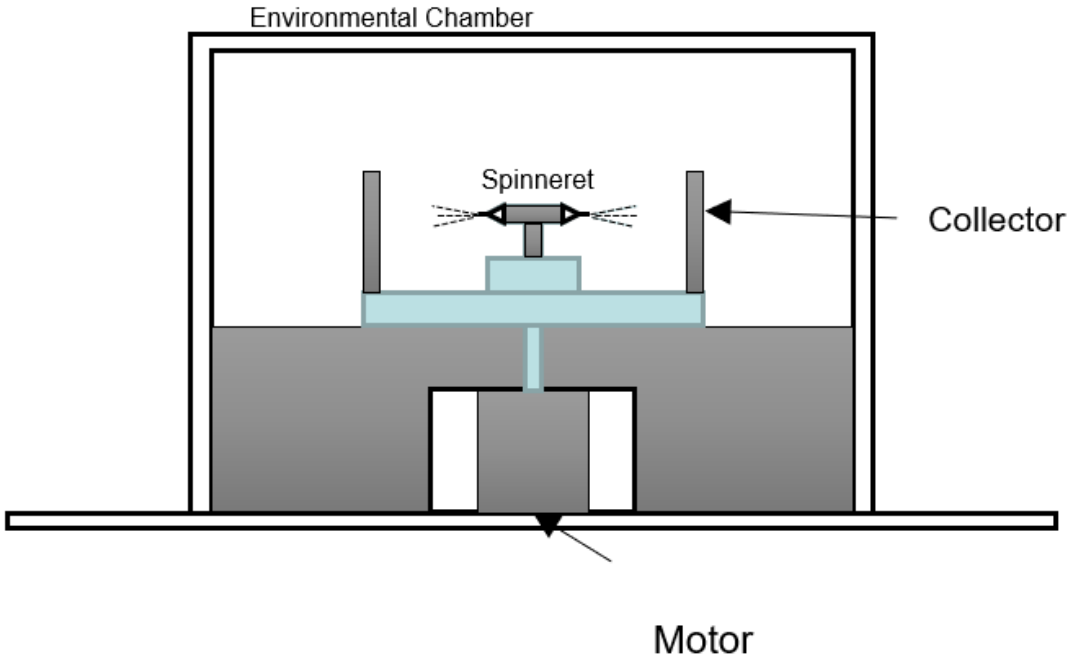

Figure 13: Schematic diagram of forcespinning setup

In the forcespinning process, the solution or melt is injected from the center of the spinneret and needles are attached to the ends of the spinneret. When the spinneret rotates with the help of

the motor, the solution or melt is ejected out of the needles due to centrifugal forces. This solution from the needles is collected on the collector in the form of nanofibers.

1.7 Poling of Piezoelectric Materials

Poling is a process of applying a high electric field across the fiber mat or film at a temperature below the melting temperature of the film. This process is done after stretching the films or fiber mats. Some of the poling methods are contact poling, corona poling, electron beam poling, photo thermal poling, photo induced poling, among others (Ting et al., 2013). Contact poling and corona poling are the most used poling methods. In contact poling, the electrodes are in contact with the piezoelectric film. The film is sandwiched between two electrodes and a high voltage is applied across the film. In some cases, the sample is poled at a higher temperature using a silicon bath.

In corona poling, a needle called corona needle is used, the film is placed on a ground electrode, and the sample is enclosed in a dome. The corona needle is suspended from the dome. The needle is not in contact with the film, a high voltage is applied to the needle. Due to the high voltage, the air in the dome is ionized, creating a charged layer on the sample thus producing a poling field across the film (Mahadeva et al., 2013). As discussed earlier, piezoelectric materials possess a dipole moment (i.e., the molecule possess partial charges). When a very high voltage is applied, the partial positive charge in the molecules is attracted to the negative high voltage source and the negative partial charge in the molecule is attracted to the high positive voltage source. Thus, the dipoles are aligned as shown in Figure 14. After the high voltage is removed, the dipoles tend to return to their original position. Due to the remanent polarization in the film, and by lowering the temperature, the dipoles are not able to return to their positions completely. Thus, the

dipoles stay somewhat aligned creating a permanent dipole moment in the material and this result is called poling.

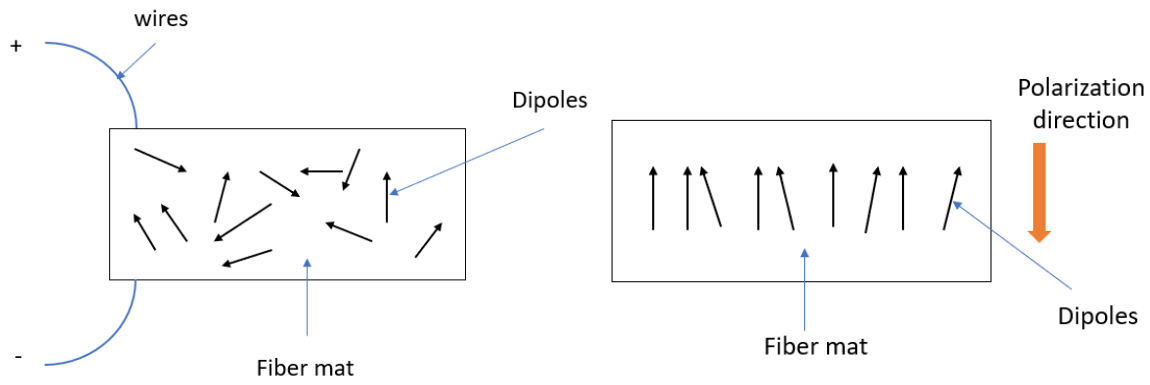

Before poling After poling

Figure 14: Effect of poling on a piezoelectric film

1.8 Energy Harvesters

Energy harvesters are devices that harness energy from environment and convert it into electric voltage. In piezoelectric energy harvesting, the transducer converts mechanical energy from the ambient environment into an electric voltage. Vibrational energy is the most commonly available and dissipated source of energy. Piezoelectric energy harvesters will harness this energy and convert it into electric voltage (Wu et al., 2013). This electric energy can be stored in energy storing units such as batteries and capacitors or can be used for required application directly.

Piezoelectric energy harvester consists of three main components: first one is the piezoelectric device which converts the ambient energy into voltage or electric potential. The

second component is a rectifier needed to make the voltage all positive. The output from the piezoelectric device is not necessarily all positive and for charging a capacitor or a battery, positive direct current is required. Therefore, rectifier converts the voltage to a positive DC voltage in order to make it suitable for charging a capacitor. The third component is the electric storage unit such as battery or capacitor. A storage unit is not needed if the electric voltage is to be used directly for the required application.

Ideally, these energy harvesters could be used in numerous applications such as micro electromechanical systems, health monitoring, sensors, smart structures, etc. Energy harvesters are important where power from the grid is not available, or it is inconvenient. Energy harvesters are a better option for biomedical applications since batteries are toxic and many piezoelectric polymers are biocompatible. Unlike traditional batteries, piezoelectric energy harvesters are not required to be charged periodically (Elahi et al., 2018). Piezoelectric energy harvesters are ideal to be used in situations where it is not possible to recharge or replace a battery for example in remote areas or in harsh environmental conditions. There have been a lot of research to improve piezoelectric energy harvesters throughout the years. Satya (2020) designed a low frequency energy harvester using PVDF. Eom et al. (2013) fabricated an energy harvester to be used for a bladder pressure sensor using parametric amplification. The energy harvester was tested as a cantilever on a shaker which tested the energy harvester at different angles of shaking (excitation angles) (Eom et al., 2013). The energy harvester generated 6 nW power with an excitation angle of 90 degrees (shaking perpendicular to the PVDF film plane) (Eom et al., 2013). Most piezoelectric energy harvesters consist of a cantilever beam or are mounted on a cantilever beam with a mass at the end to improve vibration at relatively low frequencies. The performance of the

system depends on the resonant frequency of the device. Since the energy available in the environment does not consist of only one frequency but rather multiple frequencies, it is efficient for the energy harvester to have multiple resonant frequencies. Wu et al. (2013) fabricated a piezoelectric energy harvester with 2 degrees of freedom. The device consisted of two cantilever beams, one inside the other, and this way the device had two resonant frequencies.

One of the innovative applications for piezoelectric energy harvesters is harnessing energy from moving vehicles or walking people when they ride or step on surfaces. This is possible by integrating multiple energy harvesters within the roads or walking paths. Xiong and Wang (2016) developed a novel piezoelectric energy harvester based on PZT which was integrated with a real pavement. The average power output obtained was 3.06 mW. Besides that, energy harvesters could be very important in healthcare applications. Hwang et al. (2014) fabricated a lead magnesium niobate-lead titanate (PMN – PT) piezoelectric energy harvester as a self-powered cardiac pacemaker. Artificial pacemakers are used to regulate a person's heartbeat. The device was tested successfully on a live rat. Due to the small biomechanical movements of the body, the pacemaker was able to generate 0.223 mA current and 8.2 V output. This output is enough to successfully regulate a heart without the need for an external power source. Liu et al. (2017) fabricated a self-powered sensor using electrospun PVDF for healthcare monitoring. The device was able to detect small body movements and vocal cord vibrations. The device could be used for detecting minimal muscle movements in a patient.

1.8.1 Nanogenerators.

Nanogenerators are the energy harvesters that harvest or generate energy in the form of electric voltage at a nanometer scale. Piezoelectric nanowires are commonly used for nanogenerator applications. It is predicted that the piezoelectric effect of nanowires is enhanced up to 200 - 500 % compared to bulk material. Nanowires possess higher flexibility, higher critical strain, and longer life. Nanowires are highly sensitive and could detect a very small movement or force i.e., a force at nano scale or even at a picometer scale (Wang, 2012). The first nanogenerator was presented by Wang and Song (2006). Piezoelectric zinc oxide nanowires were used for the nanogenerator.

Many researchers have been working on nanogenerators since then. Lu et al. (2009) presented a p-type phosphorous doped ZnO nanowire energy harvester. The nanowire performance was tested by applying a very small force using a conductive atomic force microscope (AFM) in contact mode. When the AFM touches the nanowires, the nanowires bend and produce a voltage of about 50 mV to 90 mV. Yu et al. (2019) fabricated a shoe pad nanogenerator using electrospun PVDF nanofibers that could harness energy during walking. They were able to obtain an output power of 6.45 μW. Jung et al. (2011) fabricated a lead-free nanowire using $NaNbO_3$ and PDMS composite. The nanowires were used after being poled along with a compressive strain rate of 0.23 %. Au/Cr coated Kapton films were used as electrodes. They were able to obtain a power density of 0.6 mW/cm^3 along with an open circuit voltage of 3.2 V and a 72 nA short circuit current. There has been notable research in nanogenerators with vertically standing nanowire arrays. The first nanogenerator presented by Wang and Song (2006) was based on vertically standing ZnO nanowire arrays. The nanowires were grown on a Al_2O_3 substrate using Au as a catalyst.

Seol et al. (2013) introduced a piezoelectric nanogenerator using a nanoforest structure. A silicon structure consisting of densely poached nanowires and nanovoids was created on a silicon substrate using metal assisted chemical etching process. This silicon structure also served as a bottom electrode. Piezoelectric $BaTiO_3$ was then deposited on the silicon structure. The top electrode was composed of Cr and Au. When subjected with external force, nanogenerators were able to produce output voltage of 0.17 V to 1.20 V. Chung et al. (2012) fabricated a ZnO film based nanogenerator. The ZnO film was directly deposited on a plastic substrate. Silver paste was used for electrode formation for the top electrode and indium tin oxide (ITO) was used for the bottom electrode. The voltage output of about 0.28 V to 0.66 V and a current density of 26.6 nA/cm^2 to 55.5 nA/cm^2 was observed with different deforming modes such as bending and rolling of the nanogenerator. The nanogenerator produces an output voltage of about 0.28 V when attached to a human hand and stretched.

1.9 Characterization Techniques for Polyvinylidene Fluoride

Multiple techniques have been developed for characterizing the phases and morphology of PVDF. Fourier transform infrared (FTIR) spectroscopy and X-ray diffraction (XRD) are commonly used techniques for characterization of phases in PVDF. Scanning electron microscopy (SEM) is one of the commonly used techniques for characterization of morphology and topography of PVDF.

1.9.1 Fourier Transform Infrared Spectroscopy.

FTIR is the most powerful tool to determine the functional groups, bonds or chemical compounds. FTIR used infrared irradiation to characterize the samples. Infrared irradiation is

produced from a black body source and passes through an interferometer. The interferogram from the interferometer is then passed through the sample. Some radiation is absorbed by the sample and the rest is transmitted. Thus, the transmission or absorbance spectra for that sample is obtained (Mohamed et al., 2017). For a particular bond in the sample, it will have one or more resonant frequencies. When the infrared is incident on this bond, the particular resonant frequency will cause the molecule to vibrate, and the bond will absorb the radiation. Thus, from the absorption spectra, the functional group or the bond in the sample can be detected.

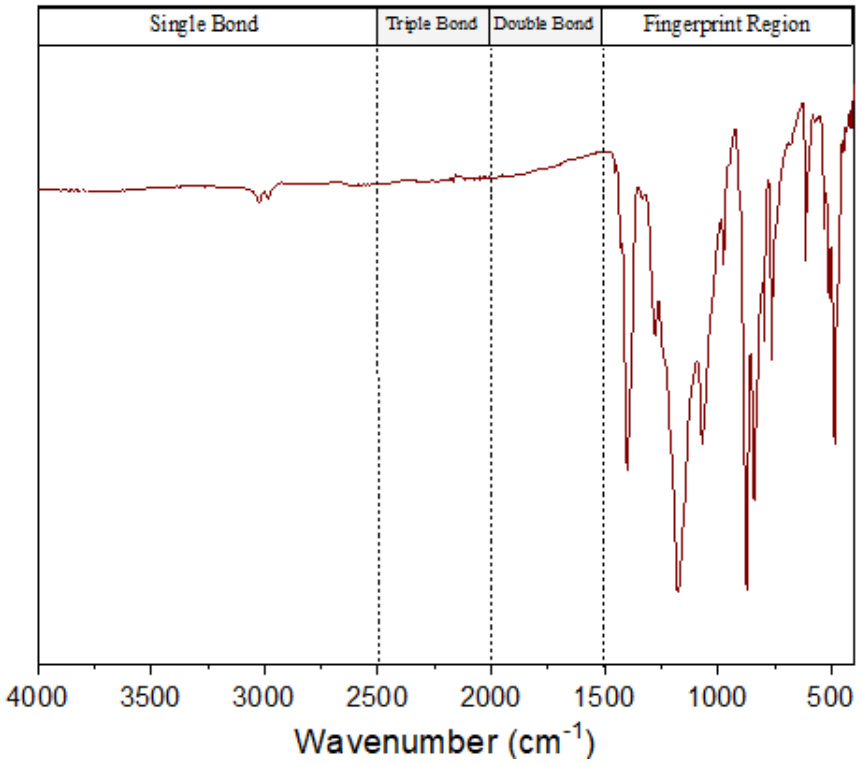

Figure 15: Fourier transform infrared spectra for polyvinylidene fluoride (PVDF) with different regions for common bond absorption region.

In PVDF, since the phases consist of different conformations, IR absorption for each phase is different. Therefore, it is possible to detect the different phases present in the PVDF sample. Figure 15 shows the four regions of the FTIR spectra for a regenerated cell membrane where the types of bonds can be analysed. The fingerprint region is for the molecules, and it is the region where phases of PVDF can be distinguished (Mohamed et al., 2017). Many researchers conflict with each other on whether a particular wave number belongs to a particular phase of PVDF (Cai et al., 2017). Absorption at wave numbers 445 cm^{-1}, 473 cm^{-1}, 1275 cm^{-1} and 1431 cm^{-1} correspond to the β-phase. Absorption peaks at 410 cm^{-1}, 489 cm^{-1}, 532 cm^{-1}, 614 cm^{-1}, 763 cm^{-1}, 795 cm^{-1}, 854 cm^{-1}, 975 cm^{-1}, 1149 cm^{-1}, 1209 cm^{-1}, 1383 cm^{-1} and 1423 cm^{-1} correspond to the α-phase. Absorption peaks at 431 cm^{-1}, 482 cm^{-1}, 776 cm^{-1}, 811 cm^{-1}, 833 cm^{-1}, 1234 cm^{-1} and 1429 cm^{-1} correspond to the γ-phase (Castkova et al., 2020; Sharafkhani & Kokabi, 2020; Yang et al., 2019; and Cai et al., 2017). Peaks at 840 cm^{-1} and 510 cm^{-1} can be associated with both β and γphases. The main peaks that can be used to differentiate between α, β and γ phases are 614 cm^{-1} and 763 cm^{-1}, 1275 cm^{-1} and 1234 cm^{-1} respectively. The fingerprint region from Figure 15 is shown in Figure 16. Here, different peaks for phases of PVDF can be seen. Dominant α peaks are seen at wavenumbers 614 cm^{-1} and 763 cm^{-1}, while, β peak around wavenumber 1275 cm^{-1} is significantly smaller. Peak at wavenumber 1234 cm^{-1}, which corresponds to the γ, is almost non-existent in this sample.

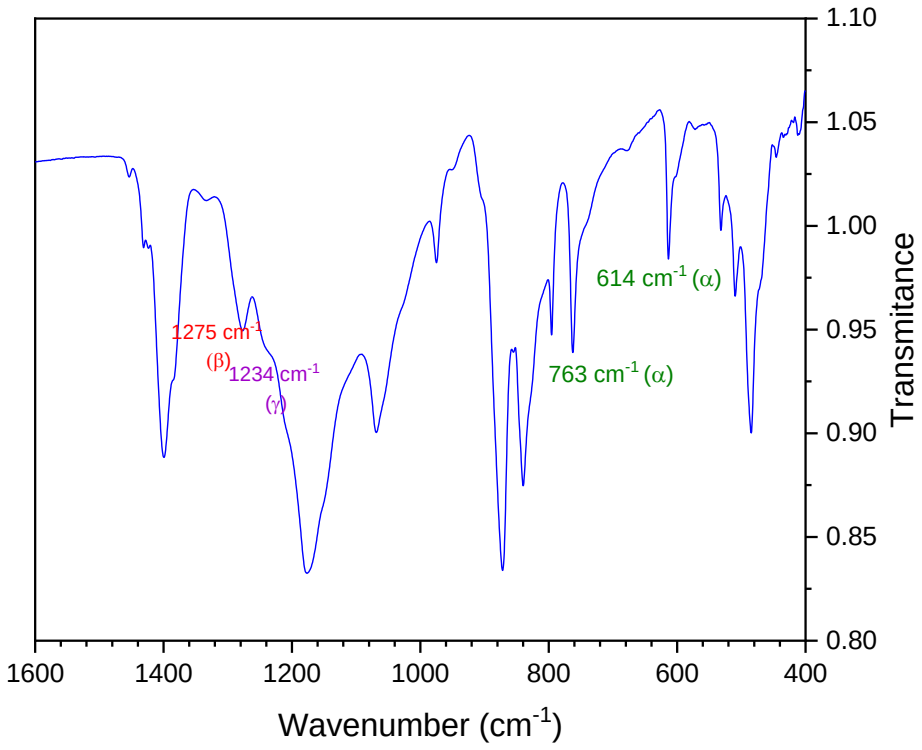

Figure 16 Fingerprint region in FTIR spectra for untreated PVDF

In a PVDF sample, the fraction of β and γ phases is given by (Castkova et al., 2020; Sharafkhani & Kokabi, 2020; and Cai et al., 2017):

$$F_{EA} = \frac{I_{EA}}{\left(\frac{K_{840}}{K_{763}}\right) I_{763} + I_{EA}} * 100\ \% \qquad (6)$$

Here, I_{EA} in the absorbance at 840 cm^{-1}, I_{763} is the absorbance at 763 cm^{-1} and K_{840} and K_{763} are the absorption coefficients with values $7.7x10^4$ cm^2/mol and $6.1x10^4$ $cm^2/$ mol,

respectively. Absorption intensities at 1275 cm^{-1} and 1234 cm^{-1} correspond to β and γ phases, respectively. Individual β and γ phase fractions can be calculated by (Cai et al., 2017):

$$F(\beta) = F_{EA} * \left(\frac{\Delta H_{\beta'}}{\Delta H_{\beta'} + \Delta H_{\gamma'}}\right) * 100\ \% \quad (7)$$

$$F(\gamma) = F_{EA} * \left(\frac{\Delta H_{\gamma'}}{\Delta H_{\beta'} + \Delta H_{\gamma'}}\right) * 100\ \% \quad (8)$$

Here, $\Delta H_{\beta'}$ is the height difference between absorption peak at 1275 cm^{-1} and the valley around 1260 cm^{-1} and $\Delta H_{\gamma'}$ is the height difference between absorption peak at 1234 cm^{-1} and the valley around 1225 cm^{-1}.

1.9.2 X-Ray diffraction.

X-Ray diffraction uses X rays to characterize the samples. When the X rays are incident on the samples, the electrons in the atoms absorb the energy and emit the same amount of energy. When the X rays are diffracted from the atoms, they create an interference pattern with each other. Interference occurs due to the path difference between the interfering X rays. For constructive interference, the path difference should be a whole number. When constructive interference occurs, it is called Bragg reflection. Bragg reflection occurs when,

$$n\lambda = 2d * \sin\theta \quad (9)$$

Here, λ is the wavelength of the X ray, θ is half the angle between the incident and the reflected rays and d is the distance between the lattice planes (Stanjek & Häusler, 2004). Therefore, as the angle θ changes, the intensity of detected X rays will change. A typical X ray spectrum shows the intensity detected X rays with respect to angle 2θ. Similar to FTIR, in XRD intensity peaks at different angles correspond to different phases of PVDF. Intensity peaks at 18.4^o, 20^o, 26.6^o, 33.2^o, 35.9^o, 38.8^o, and 41.1^o corresponding to 020, 110, 021, 130, 200, 002, and 111 reflections belongs to the α-phase of PVDF which has a monoclinic crystal structure (Castkova et al., 2020; Sharafkhani & Kokabi, 2020; Liu et al., 2013; and Cai et al., 2017). Intensity peaks at 20.6^o and 36.6^o corresponding to 110/200 and 101 reflections belong to the β-phase with orthorhombic crystal structure. Intense peaks at 20.3^o and medium peaks at 18.5^o and 39.0^o corresponding to 110/101, 020 and 211 reflections belong to the γ-phase with monoclinic crystal structure.

1.9.3 Scanning Electron Microscopy.

Scanning electron microscopy (SEM) is used for surface analysis. SEM uses an electron source which is used to emit electrons. The electrons are then accelerated using the anode. The condenser and the objective lenses are used to focus the electron beam (Inkson, 2016). When the electrons are incident on the sample, the energy from the electrons knock off the electrons from the atoms in the sample. Depending on where the electrons are knocked off from, different properties of the samples can be observed. When the scattered electrons are from the outer orbits of the atoms, they are called as secondary electrons. These electrons are detected to obtain the morphology and topographic information of the sample. The backscattered electrons are the incident electrons that are scattered at an angle more than 90^o from close to the nucleus. From

there backscattered electrons, crystallographic information about the sample can be obtained. When an electron from the inner orbit is knocked off, the electron from the higher energy orbit jumps to the lower energy orbit. This energy transition emits the energy equal to the energy difference between the orbits in form of X rays. These X rays are detected by an X ray detector. The chemical composition of the sample can be obtained using these X rays (Inkson, 2016 and Vernon-Parry, 2000).

The next chapter presents the experimental procedures for fabrication and characterization of PVDF nanofibers. Electrospinning and forcespinning are used for fabricating PVDF nanofibers. These nanofibers are then characterized using scanning electron microscopy (SEM), Fourier transform infrared spectroscopy (FTIR), and a pneumatic actuator connected to an oscilloscope for voltage response testing.

.

CHAPTER II

EXPERIMENTAL

This chapter focuses on the experimental procedure of polyvinylidene fluoride (PVDF) nanofiber fabrication along with characterization techniques.

- For nanofiber fabrication, two methods were used: electrospinning and forcespinning. These methods were used to test the effect of fabrication techniques on piezoelectricity of PVDF nanofibers.
- To test the effect of fillers in PVDF nanofibers, PVDF composite nanofibers were fabricated with BTO nanoparticles and MWCNTs using electrospinning and forcespinning.
- For characterizing the phases in PVDF nanofibers fabricated using above techniques, Fourier transform infrared spectroscopy (FTIR) was used.
- Scanning electron microscopy (SEM) was used for characterizing the PVDF nanofibers based on their morphology.
- The piezoelectric response of the PVDF nanofibers was tested using a pneumatic actuator connected to an oscilloscope. The pneumatic actuator applied pressure on the nanofibers and their voltage response is recorded using an oscilloscope.
- The nanofibers with highest piezoelectric response were then used to charge a capacitor using a vibrating machine.
-

2.1 Solution Preparation

Polyvinylidene fluoride (PVDF) pellets obtained from Kynar of grade 740 were used for the solution; N, N-Dimethylacetamide (DMA) with purity more than 99.5% from Sigma Aldrich was used as one of the solvents. Acetone was obtained from Fisher Chemical with 99.5% purity. PVDF was measured precisely using an analytical balance. 18 wt.% PVDF was dissolved in DMA and acetone with ratio 1:1. The solution was kept in a silicon oil bath on a hot plate at 60^{o}C and stirred continuously for two hours using a magnetic stirrer. This step is important in order to properly dissolve the PVDF into the solvent.

Multiwalled carbon nanotubes were used as one of the additives as it is known to increase the β-phase of the PVDF. Precisely measured multi walled carbon nanotubes were used. The MWCNTs were obtained from Sigma Aldrich with a 98% purity with 10 nm outer diameter. In this case, first 0.5% MWCNTs were added to DMA. The solution was enclosed in a vial tightly using a paraffin film. The solution was kept in an ultrasonic bath at 45 kHz for 24 hours. After ensuring that the MWCNTs are dispersed properly in DMA, PVDF and acetone was added to the solution in the same ratios as described above. The vial was then sealed again and kept in a silicon oil bath at 60 ^{o}C for two hours to insure proper dissolution of PVDF.

Samples with barium titanate (BTO) nanoparticles were prepared similar to the sample with MWCNTs. BTO nanoparticles with particle size less than 100 nm and 99% purity were obtained from Sigma Aldrich. 0.5% BTO were dispersed in DMA. The solution was kept in an ultrasonic bath at 45 kHz frequency for 1 hour. The time is much less than for the MWCNT case since proper dispersion of MWCNT took longer than that of BTO. Similar to MWCNT solution,

of PVDF was added to the solution along with acetone. The solution was then kept in a silicon oil bath at 60 ^{o}C for two hours to insure proper dissolution of PVDF.

2.2 Nanofiber fabrication:

PVDF nanofibers were fabricated using two methods: the first method was electrospinning and the second was recently developed forcespinning.

2.2.1 Electrospinning.

As discussed in chapter I, electrospinning uses a high electric field. The setup consisted of a rotating aluminium cylinder of diameter 77.6 mm, high voltage power supplies, syringe pump from KD Scientific, motor and controller for the collector, and a syringe with needle. Figure 17 shows the electrospinning setup used.

Figure 17: Electrospinning setup

First, the solution was taken out from the silicon bath and kept stationary for 5 minutes. This was done so that the air bubbles formed in the solution could escape. The solution was pulled into a syringe with 8.66 mm diameter and 3ml volume from BD Luer-Lok. A 30-gauge needle was attached to the syringe carefully. The syringe was placed on the syringe pump. A negative 15 kV voltage was applied to the collector using a carbon brush, and positive 15 kV was applied to the needle using an alligator clip. Thus, the total voltage applied between the needle and the collector was 30 kV. A 7 cm needle tip to collector distance was used. The syringe pump was set for a flow rate of 0.25 ml/hr. An aluminium collector was used and it was electrically isolated from the shaft by inserting a plastic piece between them. The speed of the collector was adjustable and up to 3500 rpm. The nanofibers were collected on the aluminium collector as shown in Figure 18. The nanofiber film was then peeled from the collector and stored in aluminium foil.

In order to test the effect of collector speed on the PVDF nanofibers, samples with DMA and acetone as solvents were electrospun at collector rotation speeds of 0 rpm, 1500 rpm, 2500 rpm and 3500 rpm. This is one set of samples. Another set of samples consisted of PVDF/MWCNT nanofibers and PVDF/BTO nanofibers with 18 wt.% PVDF with DMA and acetone as solvents in ratio 1:1 fabricated at a collector speed of 3500 rpm.

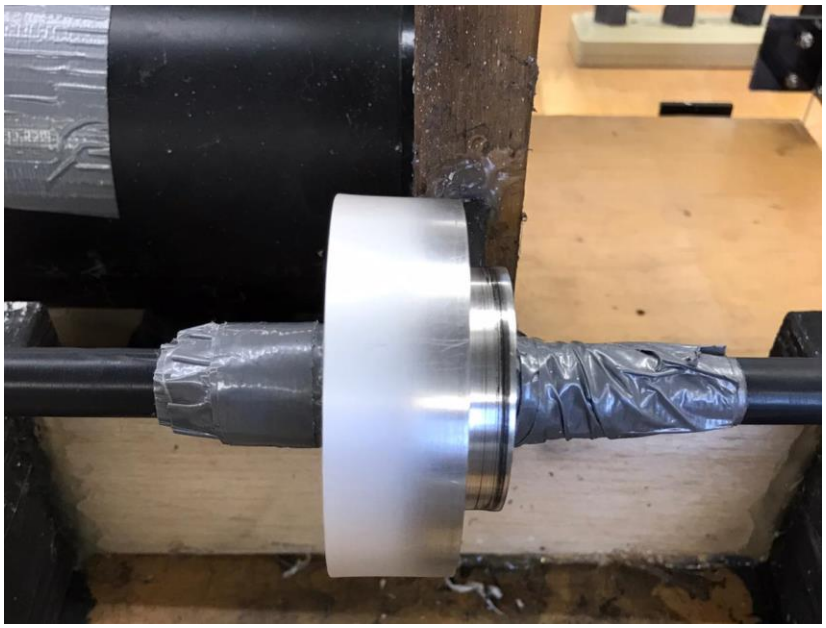

Figure 18: Nanofibers collected by electrospinning on aluminium drum

2.2.2 Forcespinning.

Figure 19 shows the inside of the forcespinning setup. The inside of the forcespinning setup is covered with aluminium prior to spinning for proper collection of fibers and for protecting the machine from the fibers and keeping it clean.

Figure 19: Preparation of forcespinning setup prior to spinning

For forcespinning, similar to electrospinning, the solution was kept stationary for 5 minutes until all the air bubbles escaped. The solution was transferred using a 3 ml syringe and an 18-gauge needle was attached to it. The solution was carefully fed into the spinneret. Two 30-gauge needles from excel international were then attached to the spinneret. Using the controller available on the Forcespinning machine, cycle specifications were selected. The solution was spun at 6000 rpm for 2 to 3 minutes. After each cycle, the fibers collected on the collector were removed using aluminium foil. The spinneret was fed with solution again, the process was repeated and new fibers were removed from collector onto an aluminium foil.

2.3 Scanning Electron Microscopy

Scanning electron microscopy (SEM) was used for analysing the morphology and diameter size of the nanofibers. Fiber mat samples were needed to be prepared for scanning, Fiber samples with size around 5 mm x 5 mm were placed carefully on the sample holder using carbon tape. In order to make the sample surface conductive, the samples were sputtered with gold using the Desk II sputter coater from Denton Vacuum. The sputtering was done in vacuum for about 80 seconds. The samples were scanned under the SEM for morphology.

2.4 Fourier Transform Infrared Spectroscopy

Fourier Transform Infrared Spectroscopy was used to characterize the samples. In FTIR, infrared radiation is passed through the sample. During this, some radiation is absorbed by the sample and some radiation is transmitted through the sample. This sample is tested for different wavenumbers. The resulting signal can be seen on the detector which shows the fingerprint if the

sample as the signal is unique for all molecules. Thus, we can detect the phases present in the sample. For FTIR, Intensity peaks at 1275 cm^{-1}, 445 cm^{-1}, 473 cm^{-1} and 1431 cm^{-1} confirms the presence of PVDF β-phase. (Cai et al., 2017)

2.5 Piezoelectric Response

The PVDR Pro machine was used to measure the electrical output of the nanofiber samples when subjected to pressure. Figure 20 shows the schematic diagram for the PVDR Pro machine. PVDR Pro consists of a pneumatic actuator arranged vertically. Bottom end of the actuator is connected to hammer which is used to apply the force and striking the piezoelectric material assembled in a sandwich between copper electrodes. The output of the nanofibers was recorded on a Tektronix TDS2012B digital oscilloscope. Figure 21 shows the setup for PVDR Pro along with the oscilloscope used. In this testing, the voltage response across the direction perpendicular to the fiber mat plane is obtained while applying mechanical stress in the same direction. Thus, the response corresponds to the d_{33} coefficient of piezoelectricity.

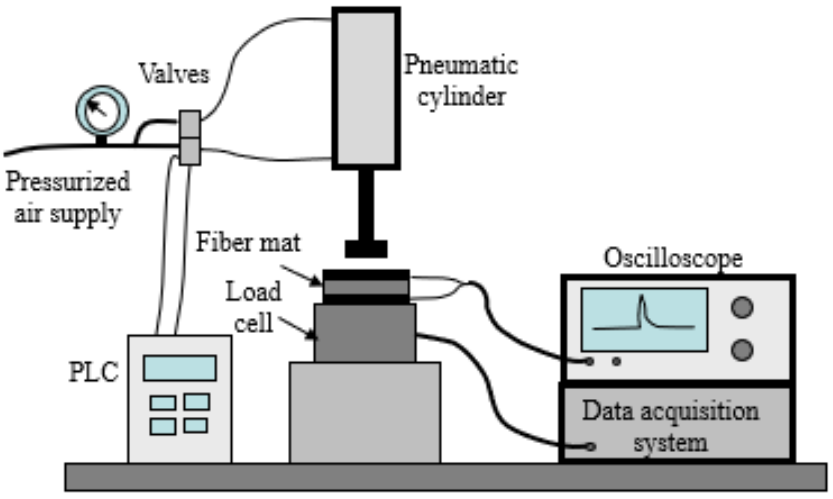

Figure 20: Schematic diagram of PVDR Pro machine

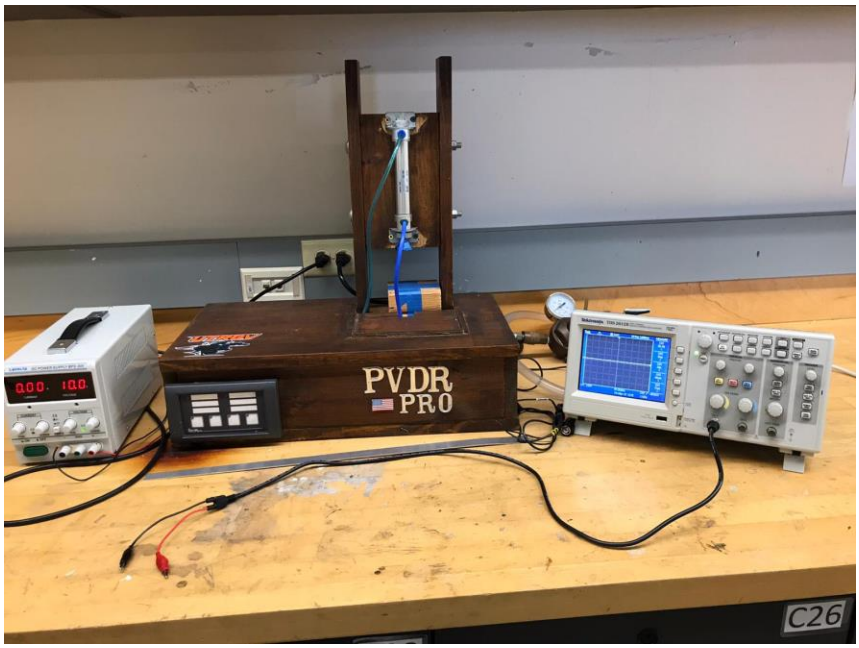

Figure 21: Setup for analysing piezoelectric response of PVDF

In the next chapter, the nanofibers with best piezoelectric response were tested for vibration energy harvesting using a vibrating machine. This voltage was then rectified and used for charging a capacitor.

CHAPTER III

FABRICATION OF ENERGY HARVESTER

This chapter focusses on construction of an energy harvesting device using Polyvinylidene (PVDF) nanofibers. Fabrication of nanofibers is explained in Chapter II. A piezoelectric energy harvesting device was fabricated and was used to harness energy from mechanical vibrations. This energy was used to charge a capacitor and then to use the stored energy to blink an LED. The steps for fabricating and testing the energy harvester are explained in this chapter.

The following steps are executed in this chapter:

- A vibrating machine is assembled for testing the PVDF nanofiber energy harvester.
- A circuit is assembled for charging a capacitor using the voltage output from the energy harvester.
- Nanofibers with the best piezoelectric response were tested using the vibrating machine for charging a capacitor.

3.1 Construction of piezoelectric energy harvester

A piezoelectric energy harvester was constructed using a nanofiber mat. There are different types of energy harvesters. In this case, a single layer mat was constructed and was mounted on a vibrating cantilever beam to function as an energy harvester. The energy harvester consists of a

PVDF nanofiber mat sandwiched between two thin copper electrodes. The electrodes are connected to wires for obtaining the electrical output. Figure 22 shows the basic construction of these energy harvesters.

Figure 22: Schematic diagram of piezoelectric energy harvester

First, the nanofiber mat is cut into desired size. The nanofiber mat was sandwiched between two copper plates ensuring that the plates do not touch each other. Two wires were connected to the copper plates for obtaining the output voltage. The whole assembly is then secured using tape. Figure 23 shows how the nanofiber PVDF mat was sandwiched between the copper plates, with a copper window were the fiber mat is placed, and the copper terminal to connect the wires.

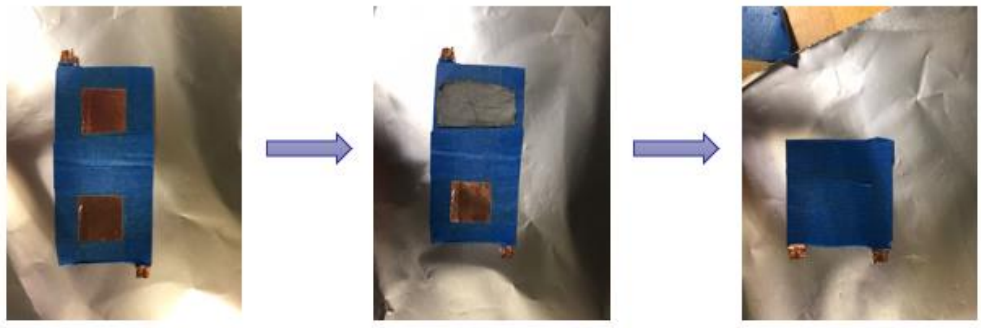

Figure 23: Process of sandwiching the nanofiber mat between two copper electrodes

3.2 Energy Harvester Testing

For testing the energy harvester explained above, a vibrating machine was assembled. A circuit is put together using a breadboard for charging a capacitor and lighting an LED.

3.3.1 Energy Harvesting Circuit.

Energy harvesting circuit is used for converting the electric output from the energy harvester to store it in a capacitor and to later use the energy to light an LED. The storing unit can be either a capacitor or a battery. The energy harvesting circuit used in this project is shown in Figure 24. The energy harvester consists of a piezoelectric device which was used for harnessing vibrational energy from the environment and convert it into electric voltage using the property of piezoelectricity. The energy harvester is connected to the rectifier. The output from the device is a bipolar DC voltage. For charging a battery or a capacitor, positive direct current (DC) is required. The rectifier is used to convert the bipolar voltage into positive DC voltage.

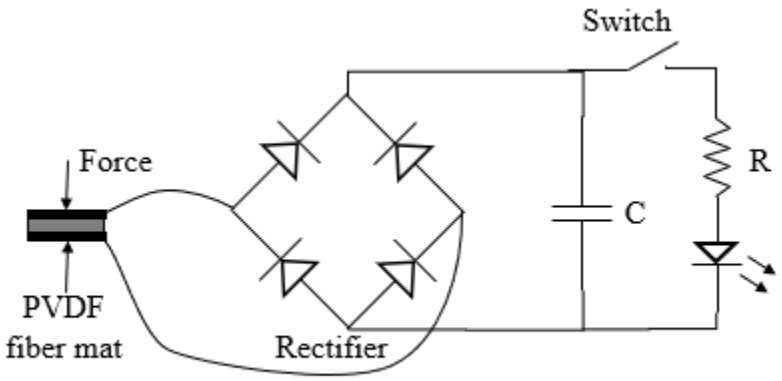

Figure 24: Capacitor charging and discharging circuit diagram

3.3.1.1 Rectifier. A rectifier is used for converting the bipolar voltage to positive DC voltage. The rectifier circuit is as shown in the Figure 25, and it consists of four diodes. A diode is an electrical equivalent of a check valve. Diode allows the flow of electric current in one direction only and blocks the current from the opposite direction. When the diode is in forward bias, current can flow through it with a small voltage drop. If the diode is in reverse bias condition, current cannot flow through it. Usually, the voltage drop across a diode is about 0.7 V.

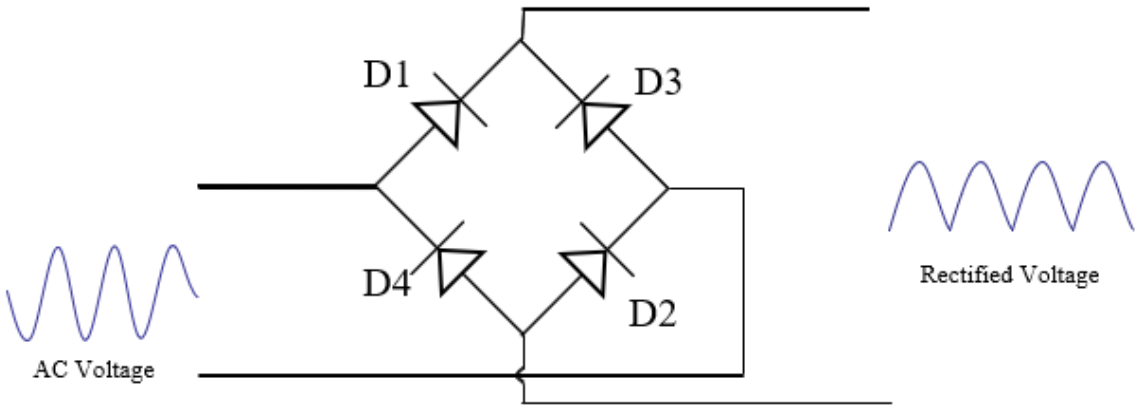

Figure 25: Rectifier circuit diagram

In the circuit shown in Figure 25, during the positive half cycle, the diodes D1 and D2 are in forward bias. The current flows from the energy harvester through diode D1, then through the output load and the diode D2 back to the energy harvester completing the circuit. During the negative half cycle, diodes D3 and D4 are forward bias. The current flows from the energy harvester device to the diode D3, then through the load, then through the diode D4 and back to the energy harvester thus completing the cycle. This type of rectifier is called a full wave bridge rectifier.

3.3.2.2 Capacitor. A capacitor is an energy storing device and the total energy stored in the capacitor is given by:

$$W = \frac{1}{2}CV^2 \tag{10}$$

where, W is the energy stored in the capacitor in joule (J), C is the capacitance of the capacitor in Farads (F) and V is the voltage across the capacitor in Volts (V). Using the above equation, for a 1000 µF capacitor to charge up to 2 volts, it would take 0.002 J of energy. The time required for the energy harvester to charge the capacitor will depend on the voltage output, current output, and the time width of the voltage pulses. The energy from the energy harvester can be calculated by:

$$E = \int I\,V dt \tag{11}$$

Here, E is the energy in Joules, I is the current in amperes (A), V is the voltage, and t is the time in seconds. Energy is the area under the power curve obtained by multiplying voltage times current. That is why the time width of the current and voltage piezoelectric response becomes important. Narrow pulses generate less energy than wide pulses during the same time length.

Figure 26 shows the circuit used for storing the voltage output from the energy harvester. A multimeter is used for measuring the voltage of the capacitor. A LED is connected as a load through a switch to use the energy stored in the capacitor. The initial idea was charging supercapacitors, but it was discovered that it will take a long time to charge them. If multiple energy harvester could be used to charge the capacitors, they will all make energy contributions and charge them faster and that might be a next step in this research project.

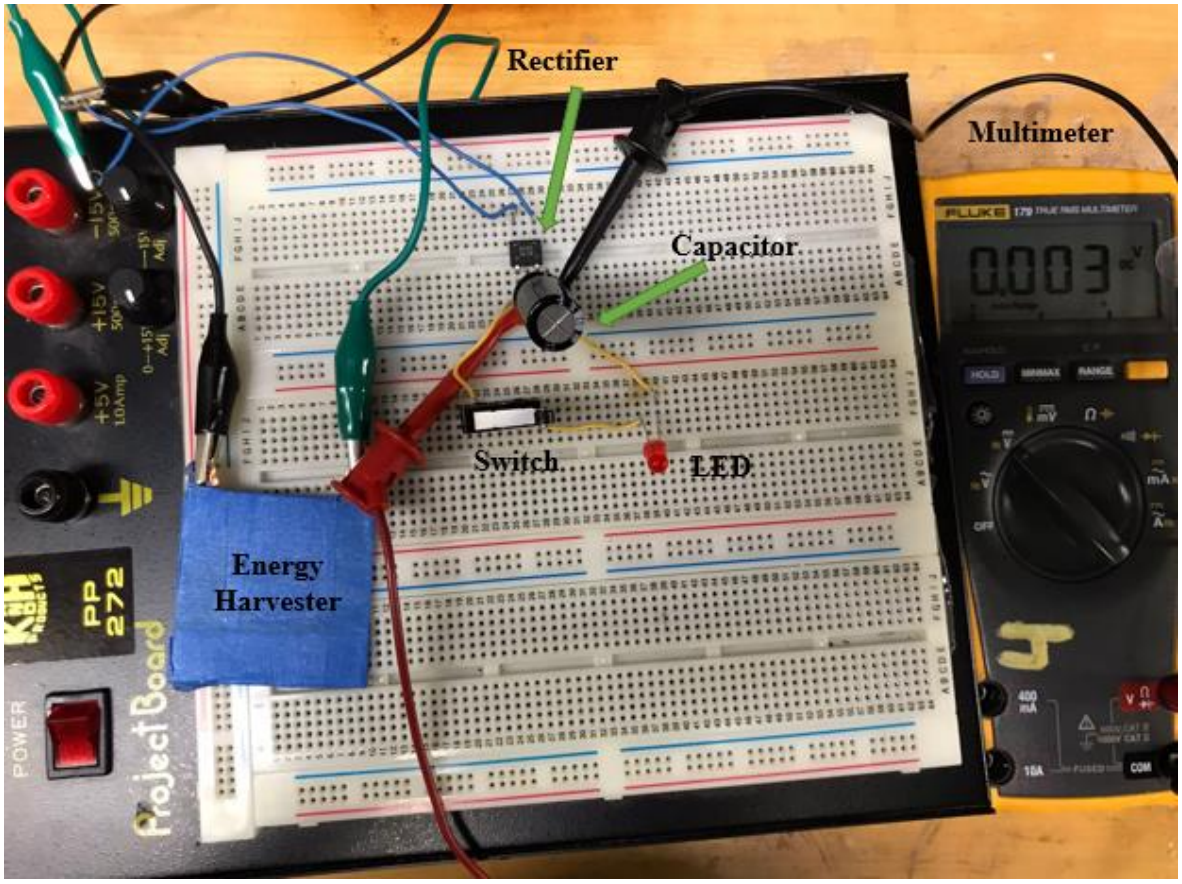

Figure 26: Capacitor charging and discharging circuit

3.3.2 Vibrating Machine.

A vibrating machine is assembled as shown in Figure 27 for charging the capacitor in the circuit above. In this assembly, the PVDF energy harvester is mounted on a cantilever beam. A cam operated by a motor is used to move the cantilever beam. When the cam rotated, it moves the cantilever thus moving the energy harvester. The cantilever is flexible enough for it to vibrate when the cam moves it. A dead load is attached to end of the piezoelectric energy harvester to insure maximum vibration. The energy harvester is connected to the circuit using wires as shown in Figure 27. While testing the nanofiber mat, the motor had to be set to a particular frequency for

optimum voltage output. This is the resonant frequency of the cantilever beam. Figure 28 shows the vibrating machine with the energy harvester and the motor.

In this experiment, the rectified output voltage was recorded. The rectified output voltage was used to charge a 1000 µF capacitor. The time required to charge the capacitor was recorded. Finally, when desired capacitor voltage was reached, the capacitor was used to light up an LED.

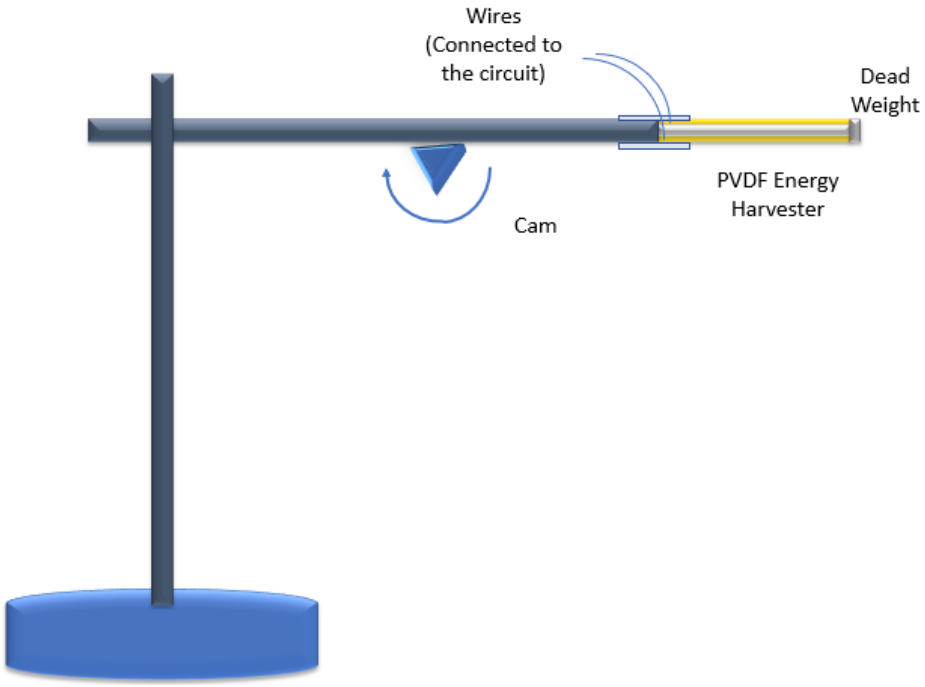

Figure 27: Schematic diagram of vibrating machine for testing the energy harvester.

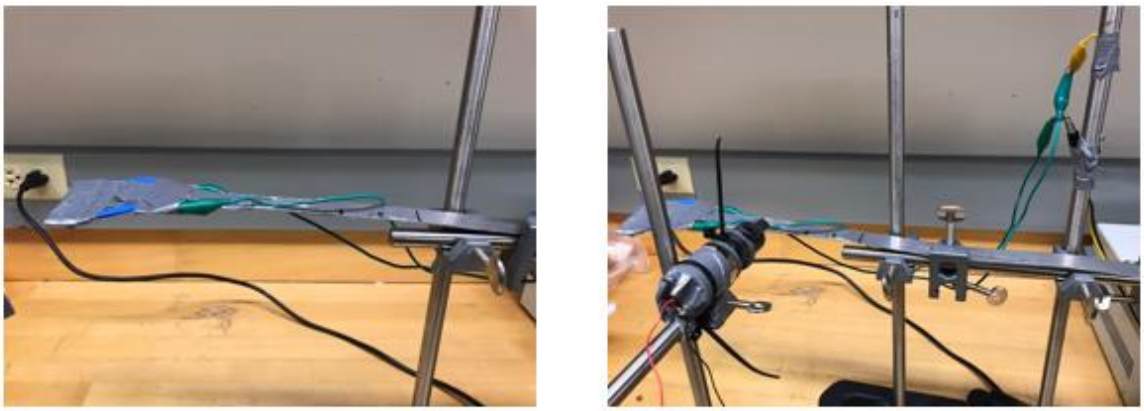

(a) (b)

Figure 28: Vibrating machine for testing the energy harvester

CHAPTER IV

RESULTS AND DISSCUSSION

4.1 Morphology of PVDF Nanofibers

4.1.1 Electrospun PVDF at different speeds.

In this section, morphology, and diameters of nanofibers for electrospun nanofibers at collector speeds of 0 rpm, 1500 rpm, 2500 rpm and 3500 rpm are discussed. The images were obtained using scanning electron microscopy (SEM). Nanofiber diameters are measured using ImageJ software and the distribution is plotted using Origin Lab software with 100 measurements for each sample.

Figure 29(a), Figure 30(a), Figure 31(a) and Figure 32(a) shows the SEM images for electrospun PVDF at collector speeds of 0 rpm, 1500 rpm, 2500 rpm and 3500 rpm respectively. It is observed that 0 rpm the nanofibers are unaligned and become more aligned as the speed increases. Figure 29(b), Figure 30(b), Figure 31(b), and Figure 32(b) shows the diameter distribution for electrospun PVDF with collector speeds 0 rpm, 1500 rpm, 2500 rpm, and 3500 rpm, respectively. There is a slight decrease in the diameter with increasing speed, although, a significant difference is not observed.

From Figure 32, with highest rpm, the mean diameter was found to be 0.614 µm with a standard deviation of 0.182 µm. Standard deviation of electrospun nanofibers is low nanofibers, indicating consistent diameter of fibers. Aligned nanofibers are observed at 3500 rpm.

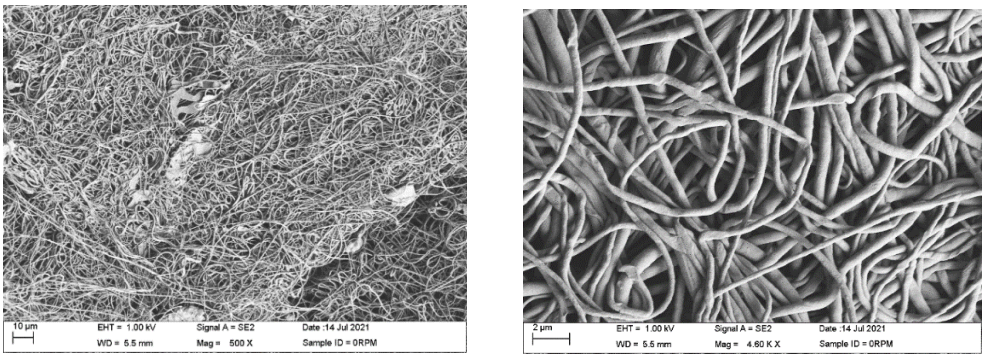

(a)

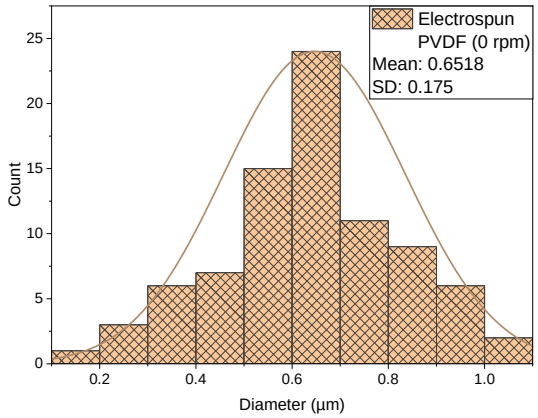

(b)

Figure 29: (a) SEM Images of electrospun PVDF at 0 rpm and (b) diameter distribution on nanofibers.

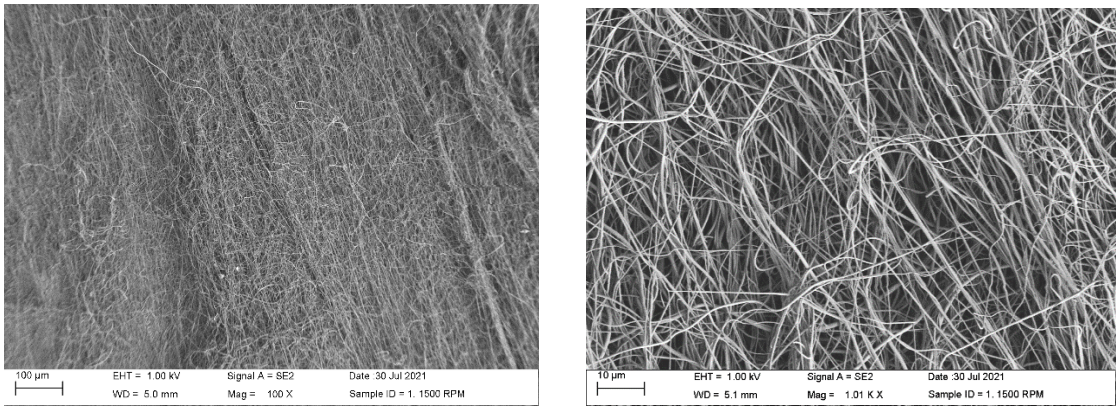

(a)

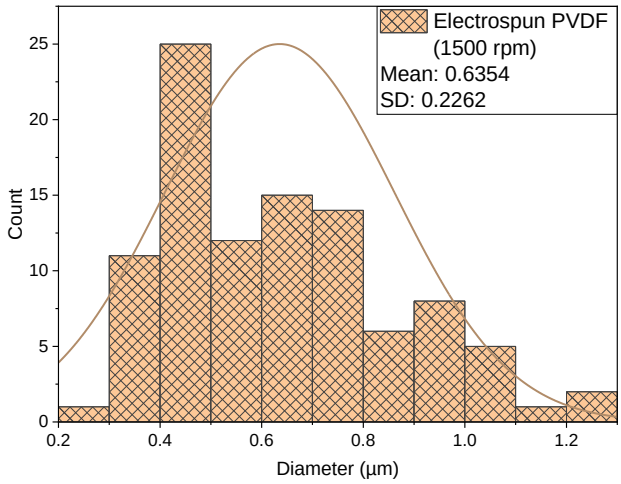

(b)

Figure 30: (a) SEM Images of electrospun PVDF at 1500 rpm and (b) diameter distribution on nanofibers

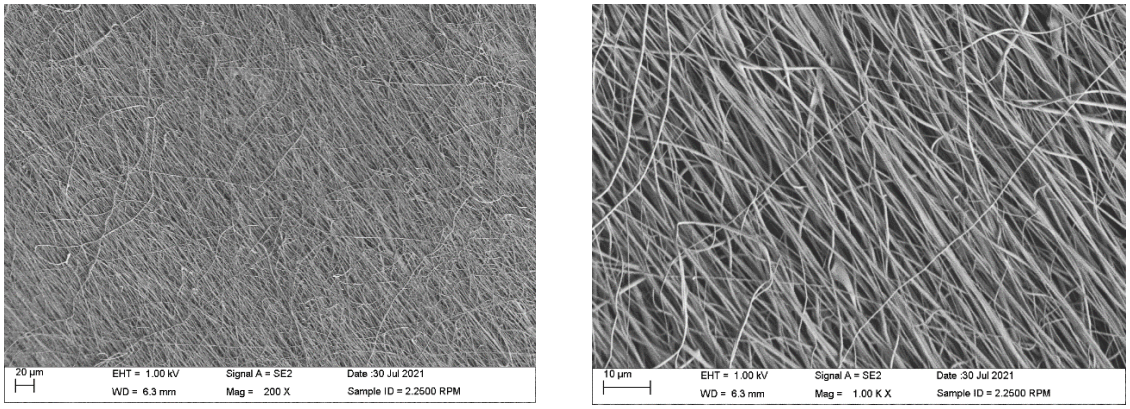

(a)

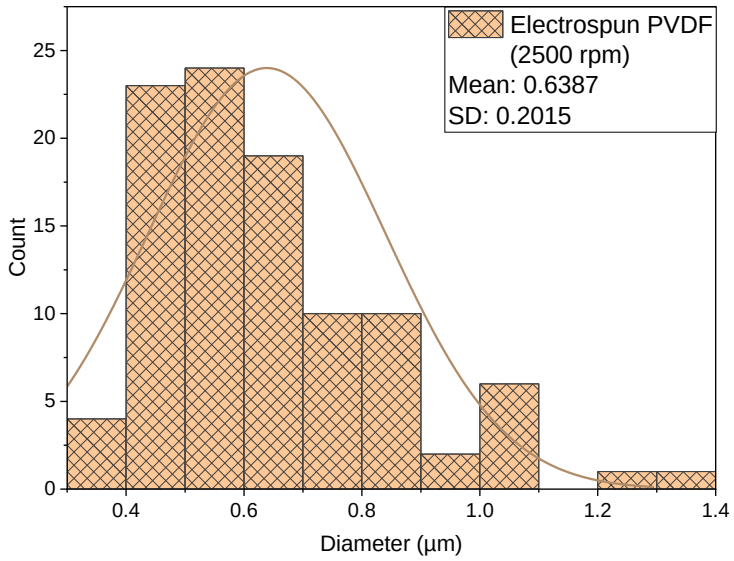

(b)

Figure 31: (a) SEM Images of electrospun PVDF at 2500 rpm and (b) diameter distribution on nanofibers

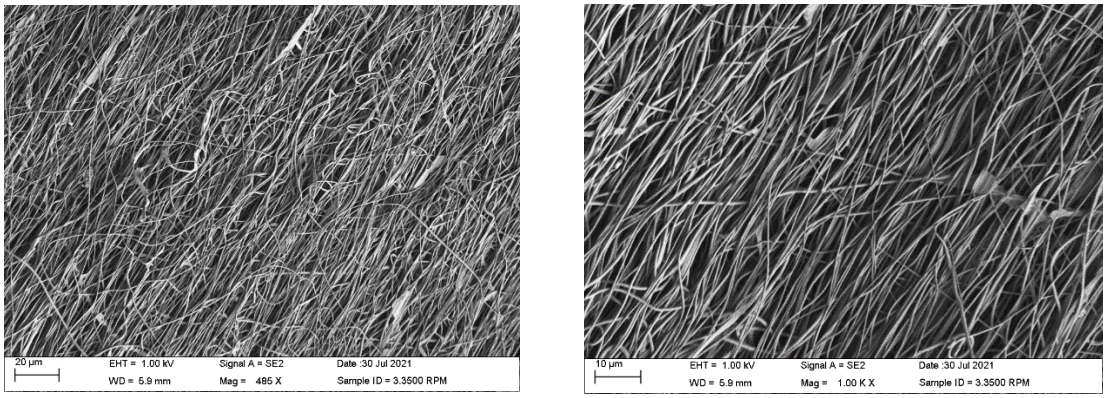

(a)

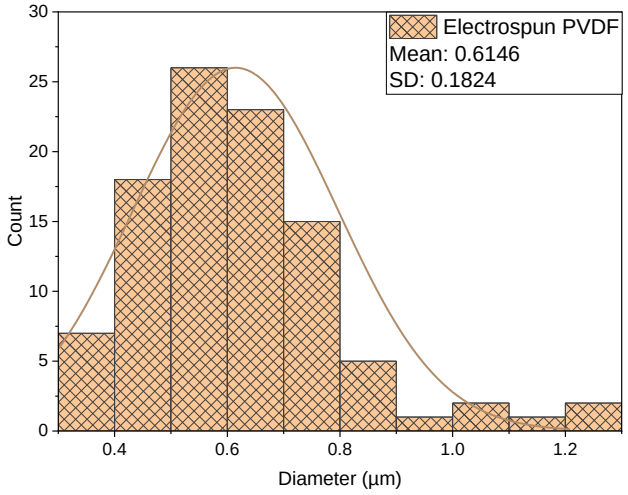

(b)

Figure 32: (a) SEM Images of electrospun PVDF at 3500 rpm and (b) diameter distribution on electrospun nanofibers.

4.1.2 Comparing electrospun and forcepun PVDF nanofibers

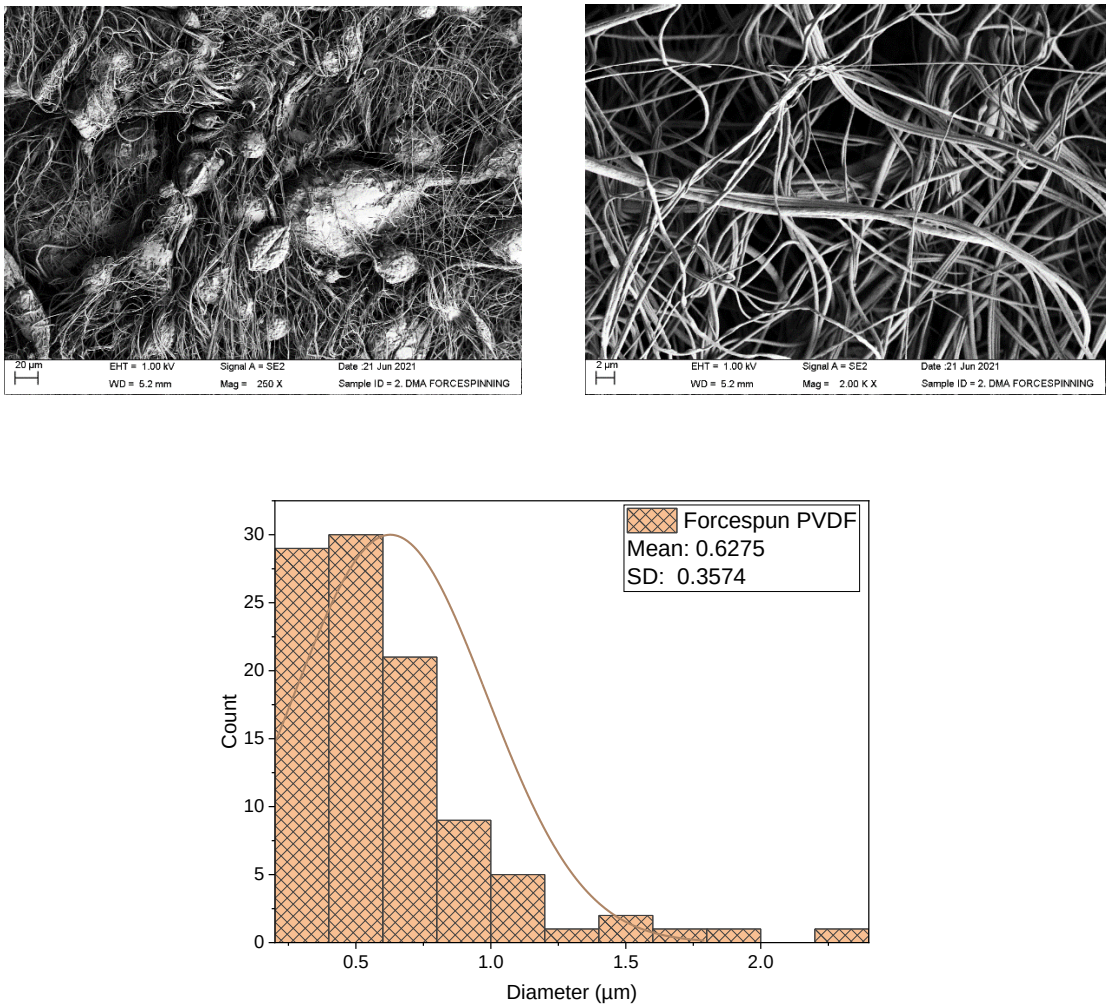

Figure 33: (a) SEM Images of forcespun PVDF and (b) diameter distribution on forcespun nanofibers.

Figure 33 shows the SEM images of samples fabricated using forcespinning. The mean diameter for forcespun PVDF was found to be around 0.627 µm with a standard deviation of 0.357 µm. Standard deviation of forcespun nanofibers is high, indicating a wide range of diameters.

Electrospun nanofibers appear to be more aligned compared to forcespun nanofibers. Also, in Figure 33, agglomeration of PVDF is observed. No such agglomeration is observed in the SEM

image of electrospun nanofibers. Similar agglomeration of PVDF is observed in numerous forcespun samples but none of the electrospun samples. Additional SEM images and mean diameters of several samples are given in the APPENDIX.

4.2 Piezoelectric Phases and Response in Electrospun and Forcespun PVDF Nanofibers.

In this section, the Fourier transform infrared spectroscopy (FTIR) results are discussed for the nanofibers. Electrospun and forcespun nanofibers with and without nanoparticles are discussed. All the electrospun nanofibers in this section are spun at a collector speed of 3500 rpm.

4.2.1 FTIR Results for Electrospun Nanofibers

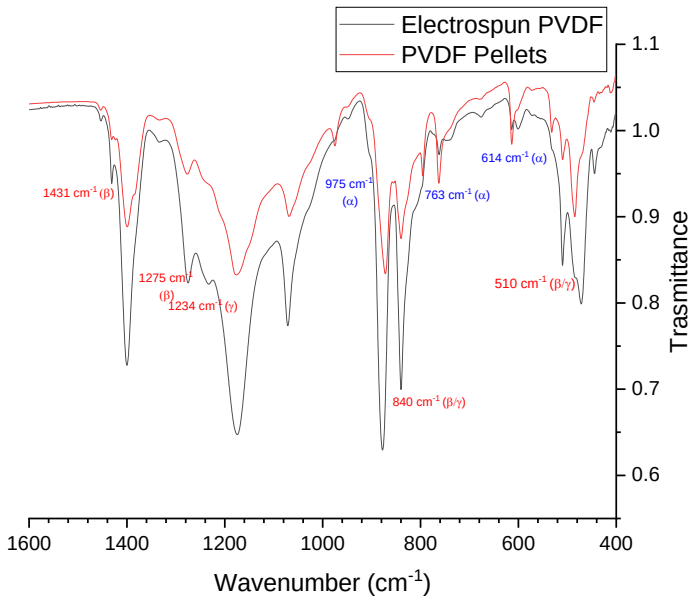

Figure 34: FTIR spectra for raw PVDF and Electrospun PVDF

Figure 34 shows the FTIR spectra for PVDF nanofibers fabricated using electrospinning. Phases in PVDF were studied using FTIR. Figure 34 shows the FTIR spectra for PVDF nanofibers fabricated using electrospinning using solvents DMA and acetone. Peaks around 881 cm^{-1}, 1071 cm^{-1}, 1175 cm^{-1}, and 1401 cm^{-1} are present in all PVDF samples. Peak at 1275 cm^{-1}, is an indication of presence of β phase in the sample. This peak appears to be present in both samples. Peaks around 445 cm^{-1}, 473 cm^{-1} and 1431 cm^{-1} also correspond to the β phase which is present in both samples. Peaks around 410 cm^{-1}, 532 cm^{-1}, 614 cm^{-1},762 cm^{-1} and 975 cm^{-1} correspond to the α phase. Peaks around 430 cm^{-1} and 1232 cm^{-1} correspond to the γ phase. Peaks at 840 cm^{-1} and 510 cm^{-1} could be assigned to either β or γ phase.

Comparing the electrospun samples and raw PVDF, it can be seen that the α peaks at 410 cm^{-1} and 614 cm^{-1} in electrospun sample are small compared to PVDF pellets. α peaks at 532 cm^{-1}, 795 cm^{-1} and 975 cm^{-1} seems to be vanishing in the electrospun sample. β peaks at 1431 cm^{-1} and 1275 cm^{-1} are clearly higher in electrospun sample. In a PVDF sample, peaks at 489 cm^{-1}, 473 cm^{-1}, and 482 cm^{-1} correspond to α, β and γ phases respectively. In raw PVDF the peak is observed at 485 cm^{-1} indicating the presence of α phase. In the electrospun sample, the peak shifts towards 475 cm^{-1} indicating a dominant β phase.

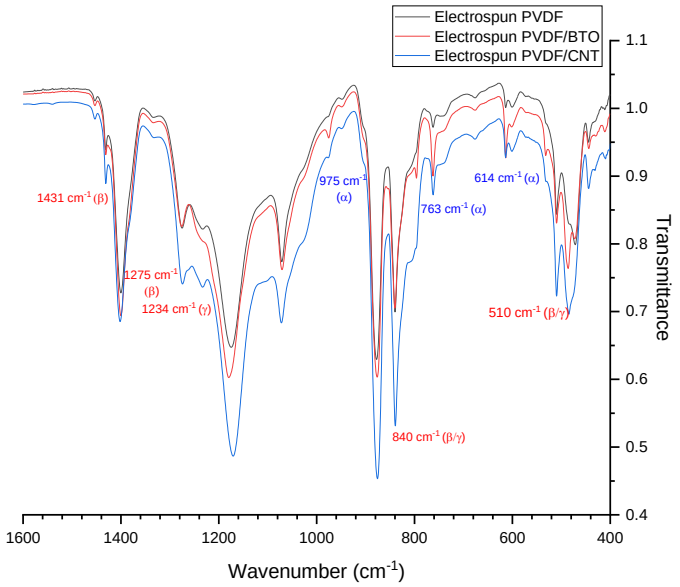

Figure 35: FTIR spectra for Electrospun PVDF with DMA solvent (BTO: Barium Titanate and CNT: Carbon Nanotubes)

Figure 35 shows the FTIR spectra for PVDF nanofibers fabricated using electrospinning with solvent DMA and different nanoparticles. Peaks at 1275 cm^{-1}, 445 cm^{-1}, 473 cm^{-1}, and 1431 cm^{-1} corresponding to β phase are present in all samples. β peaks at 445 cm^{-1} and 1275 cm^{-1} are more prominent in DMA sample than other samples. Peaks at 410 cm^{-1}, 531 cm^{-1}, 614 cm^{-1} and 763 cm^{-1} corresponding to α phase are present in all samples. These peaks are significantly smaller in DMA sample. α peaks at 795 cm^{-1}, 975 cm^{-1}, and 532 cm^{-1} are present in other samples but vanished from DMA sample. Peaks at 489 cm^{-1}, 473 cm^{-1}, and 482 cm^{-1} correspond to α, β and γ phases respectively. In DMA sample, the peak from 485 cm^{-1} shifts toward 473 cm^{-1}. This indicated decrease in α and γ phases and increase in β-phase. β-phase appears to be more prominent with CNT additives when compared to BTO additives.

4.2.2 FTIR Results for Forcespun Nanofibers

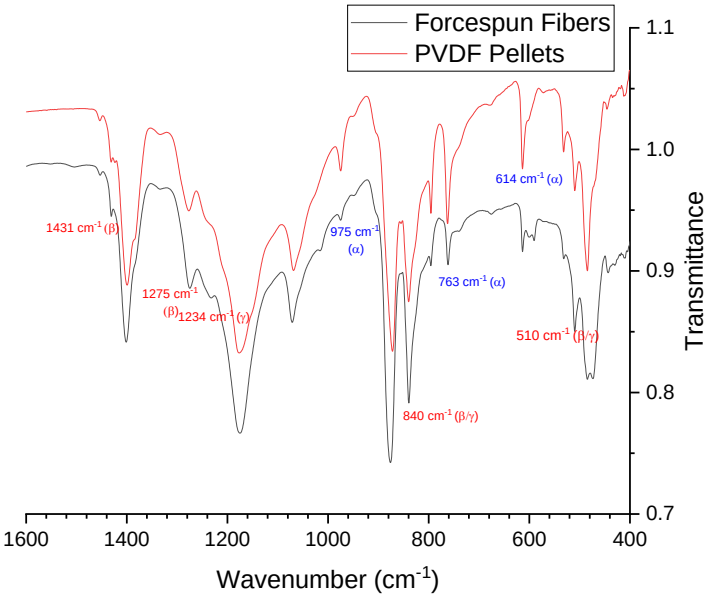

Figure 36: FTIR spectra for raw PVDF and Forcespun PVDF

Figure 36 shows the FTIR spectra for PVDF nanofibers fabricated using forcespinning and PVDF pellets. Common peaks around 881 cm^{-1}, 1071 cm^{-1}, 1175 cm^{-1}, and 1401 cm^{-1} seen in all PVDF samples are present. Peak around 1234 cm^{-1} is present in both samples. This peak is an indication of presence on piezoelectric γ phase. Peak at 431 cm^{-1} also corresponds to the γ phase. Peak at 1275 cm^{-1} corresponding to the β phase is present in both samples. Other peaks corresponding to β phase around 445 cm^{-1}, 473 cm^{-1}, and 1431 cm^{-1} are also present in both samples. Peaks at 510 cm^{-1} and 840 cm^{-1} corresponds to either β or γ phase. α phase peaks around 614 cm^{-1}, 763 cm^{-1}, 410 cm^{-1}, 532 cm^{-1}, 795 cm^{-1} and 975 cm^{-1} are present in both samples. α peaks at 410 cm^{-1} and 614 cm^{-1} in forcespun sample are small compared to PVDF pellets. α peaks at 532 cm^{-1}, 795 cm^{-1} and 975 cm^{-1} seems to be almost vanishing in the forcespun sample. α peak at 485 cm^{-1} in PVDF pellets shifts towards the β peat at 475 cm^{-1} in the forcespun sample.

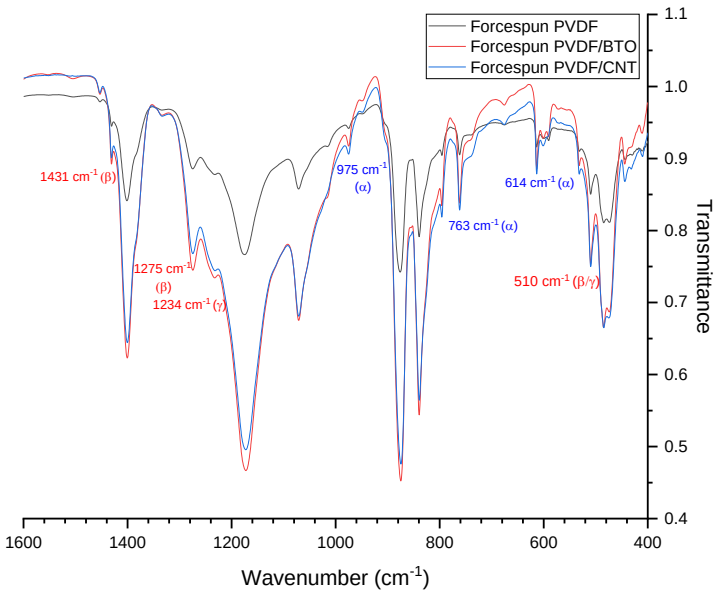

Figure 37: FTIR Spectras for Forcespun PVDF with DMA solvent (BTO: Barium Titanate and CNT: Carbon Nanotubes)

Figure 37 shows the FTIR spectra for PVDF nanofibers fabricated using forcespinning using DMA and acetone as solvents as explained in Section II. FTIR spectra for three samples are compared here: one without nanoparticles, second with barium titanate (BTO) and third with multi-walled carbon nanotubes (MWCNTs). In Figure 37 the sample without any nanoparticles seem to have very low absorption overall. Peaks around 410 cm^{-1}, 489 cm^{-1}, 531 cm^{-1}, 614 cm^{-1}, 763 cm^{-1}, and 975 cm^{-1} correspond to the α phase. Peaks around 1275 cm^{-1}, 445 cm^{-1}, 473 cm^{-1}, and 1431 cm^{-1} correspond to the β phase. Absorption peaks around 431 cm^{-1}, 482 cm^{-1}, and 1234 cm^{-1} correspond to the γ phase. Absorption peaks around 510 cm^{-1} and 840 cm^{-1} can be assigned to either β or γ phase. Significant difference between absorption peaks is not observed between samples with nanoparticles and sample with MWCNTs.

Results of FTIR analysis are summarized in Table 2. A very high amount of β-phase is obtained with electrospun PVDF. The percentage of β-phase clearly increased from 61.8 % in bulk to 75.7% in electrospun PVDF. Addition of BTO or MWCNT is electrospun PVDF did not increase the percentage of β-phase, rather, it decreased.

Percentage of β-phase seems to have decreased in forcespun PVDF than bulk PVDF. Addition of MWCNT and BTO improved the percentage of β-phase in forcespun nanofibers. Difference between forcespun PVDF/BTO and forcepun PVDF/MWCNT is not significant.

Table 2: Amount of piezoelectric phases in electrospun and forcespun PVDF

Sample	Amount of β + γ phase	Amount of β phase	Amount of γ phase
Bulk PVDF	61.8 %	61.8 %	0 %
Electrospinning			
PVDF	89.5 %	75.7 %	13.8 %
PVDF/BTO	70.0 %	70.0 %	0 %
PVDF/MWCNT	74.3 %	47.8 %	26.5 %
Forcespinning			
PVDF	63.5%	57.1 %	6.5 %
PVDF/BTO	69.4 %	63.8 %	5.6 %
PVDF/MWCNT	67.1 %	63.5 %	3.6 %

4.2.3 Voltage Responses of Electrospun PVDF.

In this section, the voltage responses of the electrospun nanofibers are discussed. The PVDR Pro machine was used for measuring the voltage response of the nanofibers. The PVDF nanofibers were sandwiched between two copper plates. The nanofibers were tested with a pressure of 20 psi (0.138 MPa). The results for different nanofibers are given below. These results correspond to the d_{33} coefficient of piezoelectricity and discussed in section 2.6.

From Figure 39 and Figure 40, it is observed that voltage response of sample with BTO nanoparticles is much higher than that with MWCNTs. Although, these voltage responses are smaller than sample without any nanoparticles shown in Figure 38. These results correspond to the FTIR results listed in Table 2. The electrospun PVDF nanofibers with highest β-phase of 75.7 % produced the highest voltage of 41 V. These voltage responses are summarized in Table 3.

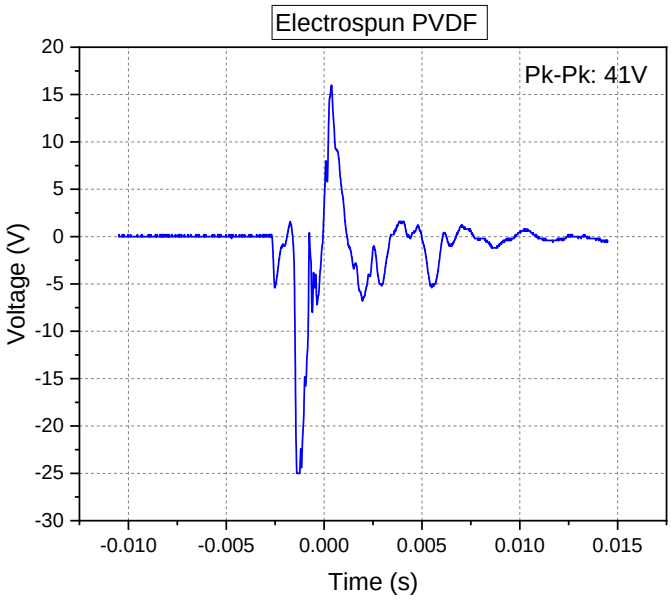

Figure 38: Voltage Response for Electrospun PVDF

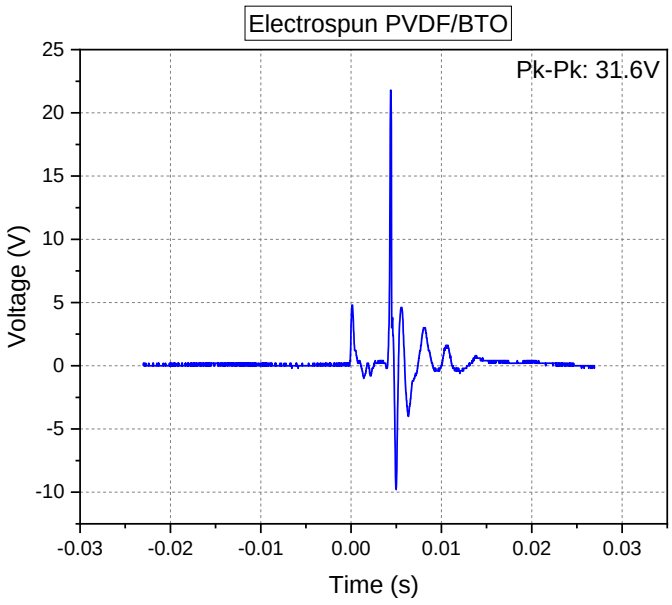

Figure 39: Voltage Response for Electrospun PVDF with BTO nanoparticles

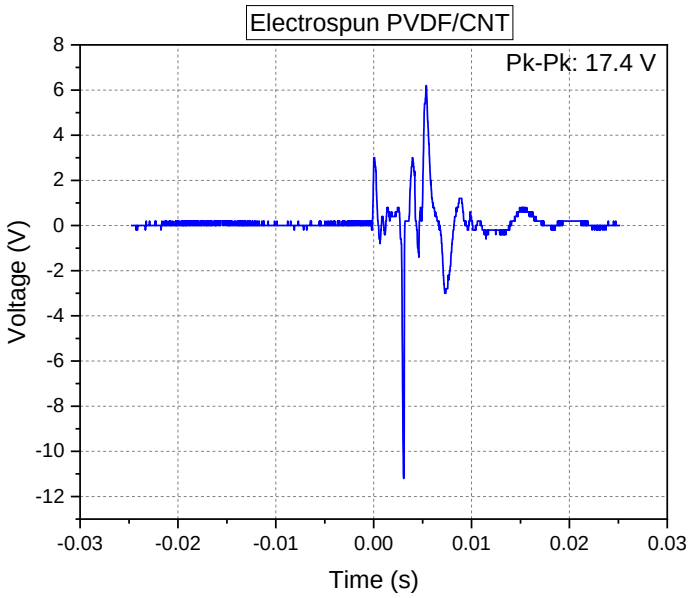

Figure 40: Voltage Response for Electrospun PVDF with MWCNTs

4.2.4 Forcespun PVDF with MWCNTs and BTO nanoparticles.

In this section, the voltage responses of the forcespun nanofibers are discussed. Similar electrospun nanofibers in previous section, the PVDR Pro machine was used for measuring the voltage response of the nanofibers with a pressure of 20 psi.

Figure 41, Figure 42 and Figure 43 shows the voltage responses for Forcepun PVDF, PVDF/BTO and PVDF/MWCNTs respectively. Voltage responses of PVDF/BTO and PVDF/MWCNTs are higher than PVDF alone. This corresponds to the FTIR results shown in Table 2. The highest voltage is obtained with PVDF/MWCNTs. This confirms that addition of BTO and MWCNTs increase the piezoelectricity in forcespun PVDF. The voltage responses are summarized in Table 3.

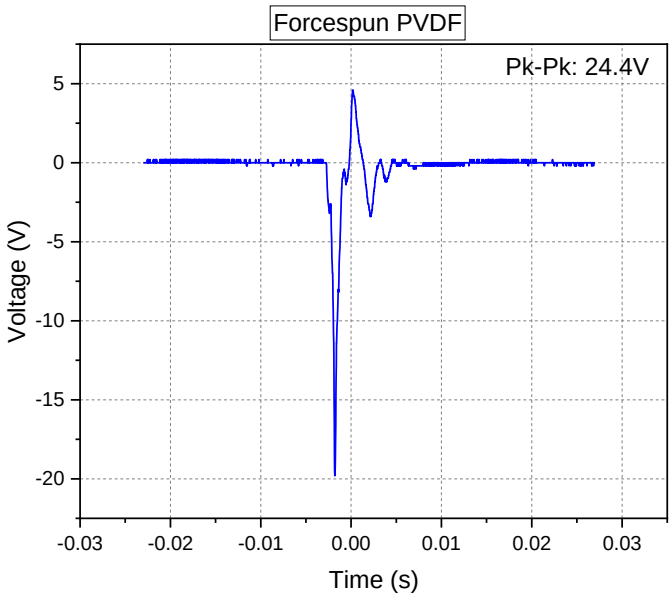

Figure 41: Voltage Response for Forcespun PVDF

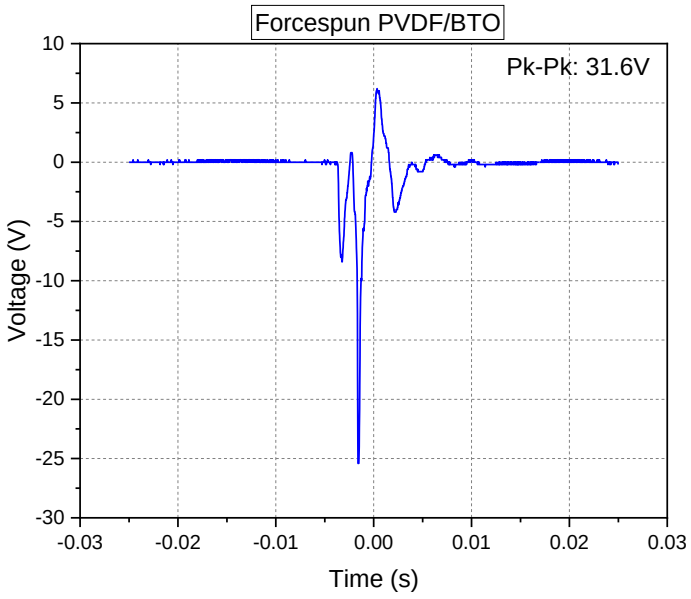

Figure 42: Voltage Response for Forcespun PVDF with BTO nanoparticles

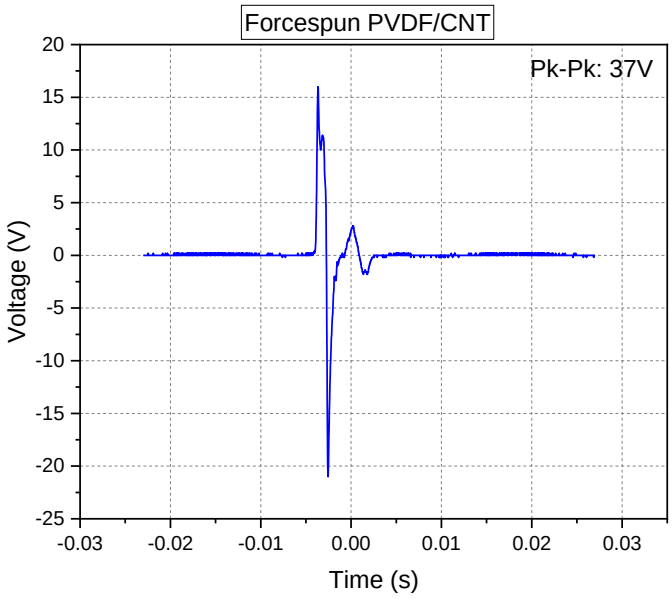

Figure 43: Voltage Response for Forcespun PVDF with MWCNTs

.

Table 3: Voltage response of different PVDF nanofiber mats

Sample No.	Sample Name	Voltage Output (V)
Electrospinning		
1	No nanoparticles	41 V
2	BTO nanoparticles	31.6 V
3	MWCNTs	17.4V
Forcespinning		
4	No Nanoparticles	24.4 V
5	BTO nanoparticles	31.6 V
7	MWCNTs	37 V

4.3 Piezoelectric Response of Electrospun PVDF nanofibers at Varying Speeds

The voltage responses of electrospun PVDF nanofibers at collector speeds of 0 rpm, 1500 rpm, 2500 rpm and 3500 rpm are discussed in this section. The PVDR Pro machine was used for measuring the piezoelectric response of the nanofibers. The nanofibers were tested with a pressure of 20 psi (0.138 MPa).

The voltage responses of PVDF nanofibers at varying collector speeds are summarized in Table 4. It is observed that the highest voltage response was obtained with a collector speed of 3500 rpm. Voltage responses increase with increasing collector speeds. One of the ways to induce β-phase in PVDF is stretching. Increasing collector speeds increases the stretching of PVDF nanofibers, therefore, increasing β-phase which in turn increases the voltage output of the nanofibers.

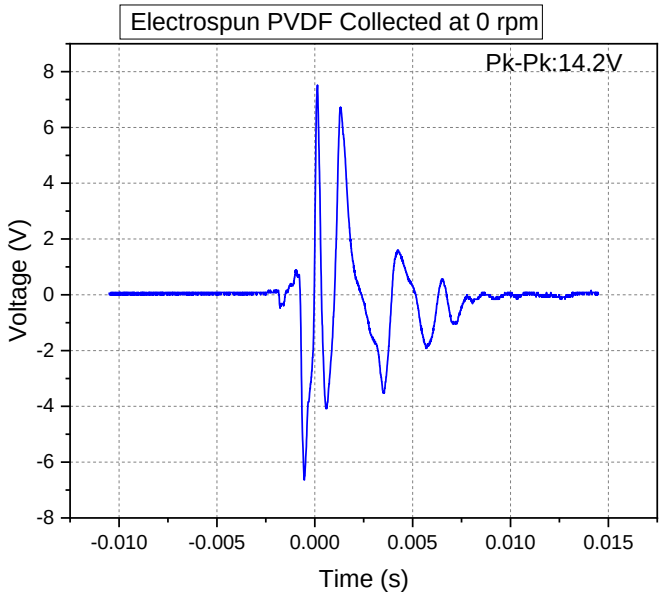

Figure 44: Voltage Response electrospun PVDF at 0 rpm collector speed

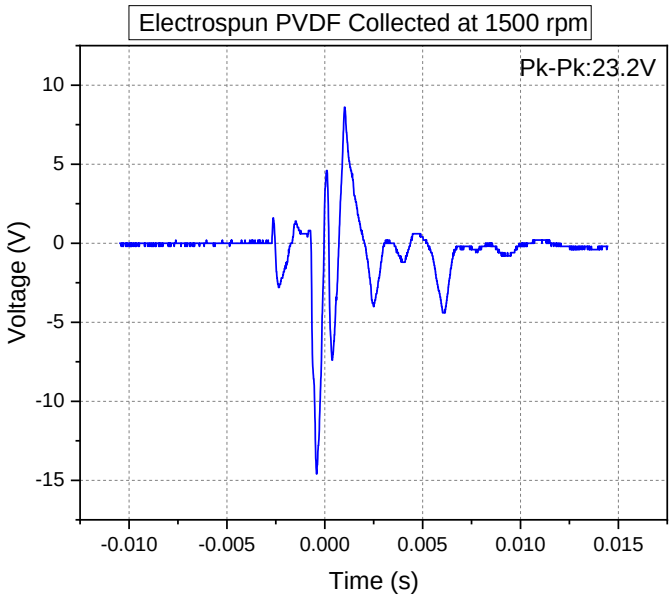

Figure 45: Voltage Response electrospun PVDF at 1500 rpm collector speed

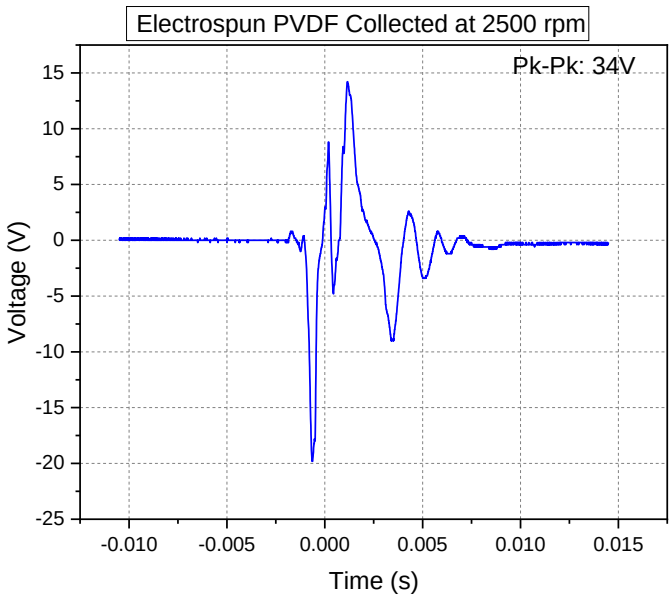

Figure 46: Voltage Response electrospun PVDF at 2500 rpm collector speed

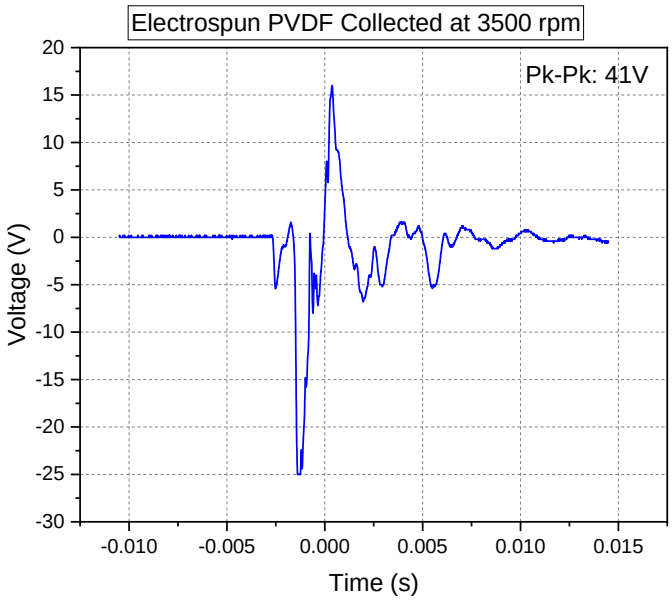

Figure 47: Voltage Response for electrospun PVDF at 3500 rpm collector speed

Table 4: Voltage responses for electrospun PVDF at varying collector speeds

Sample No.	Collector Speed	Peak-to-peak Voltage Output (V)
1	0 rpm	14 V
2	1500 rpm	23 V
3	2500 rpm	34 V
4	3500 rpm	41 V

4.4 Piezoelectric Energy Harvester

The energy harvester was tested using the vibrating machine explained in section III. In this experiment, the voltage response is due to bending of the nanofibers. Therefore, the deformation of fibers is assumed to be along to the fiber mat plane in the direction of the cantilever beam. The voltage is measured in direction perpendicular to the fiber mat plane. Thus, the response of the vibrations corresponds to the d_{31} piezoelectric coefficient as opposed to the d_{33} coefficient in PVDR Pro testing in section 4.3. Hence, in this testing, forcespun PVDF/MWCNT composite nanofiber mat provided better voltage response of 24.8 V to vibrations than the electrospun PVDF which produced 10.6 V.

Figure 48 shows the response of the energy harvester voltage output with forcespun PVDF/MWCNT. A voltage of 24.8 V was obtained at the frequency of around 8 Hz. This is the resonant frequency of our energy harvester. In order to charge a capacitor, the output of the energy harvester has to be rectified. A full wave bridge rectifier is used for this purpose. The rectified output is shown in Figure 49.

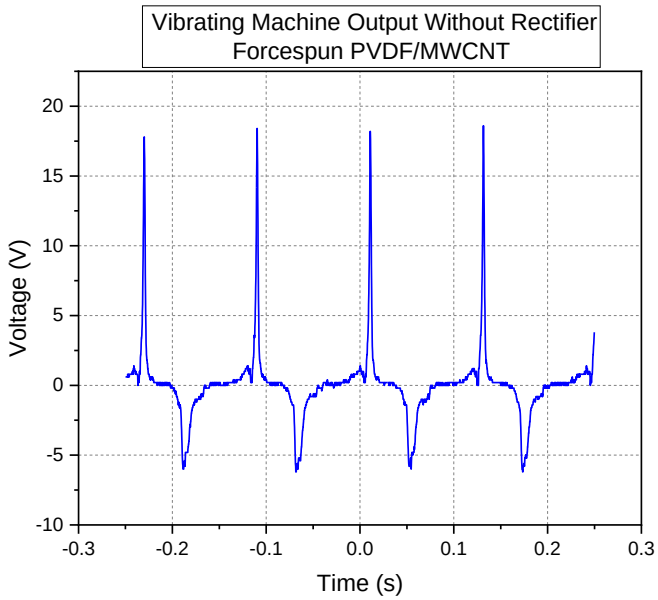

Figure 48: Forcespun PVDF/MWCNT energy harvester response before the rectifier

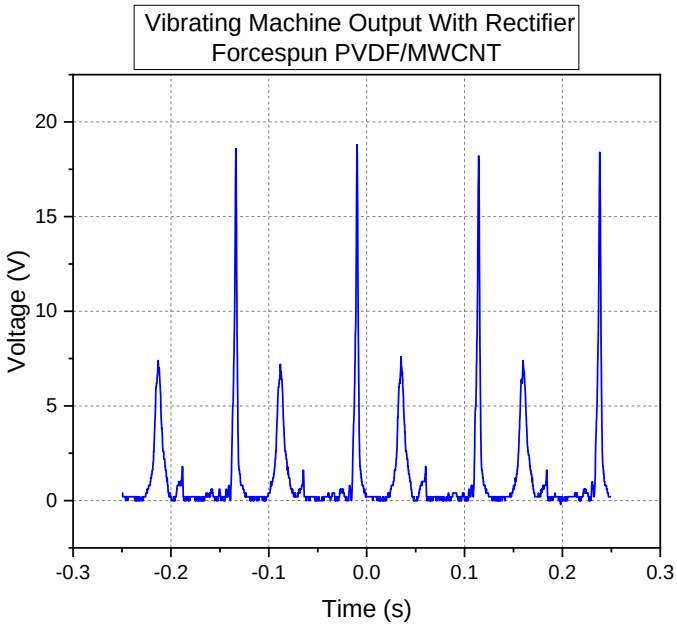

Figure 49: Forcespun PVDF/MWCNT energy harvester response after the rectifier

Using the circuit explained in section III, a 1000µF capacitor is charged using this energy harvester. Figure 50 shows the capacitor charging over time. The capacitor charges around 30 mV every 30 seconds.

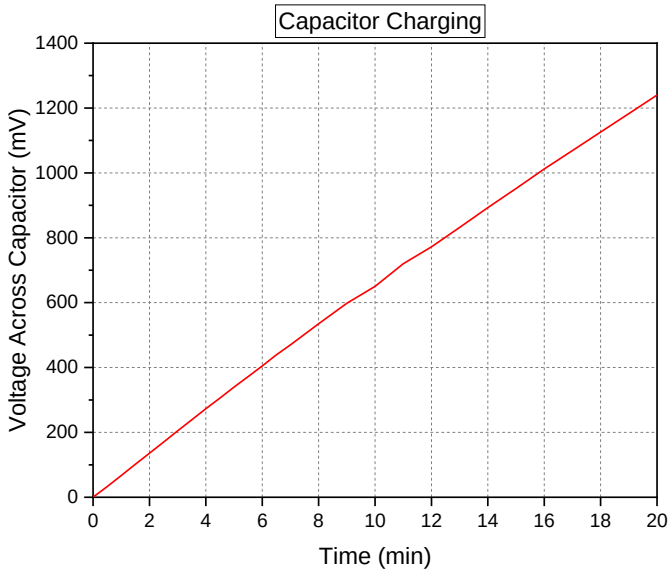

Figure 50: Capacitor charging due to the forcespun PVDF/MWCNT energy harvester

Electrospun PVDF was also tested using the vibrating machine. Figure 51 shows the response of the energy harvester voltage output with electrospun PVDF. An output voltage of 10.6 V was obtained. Figure 52 shows the rectified output from the vibrating machine.

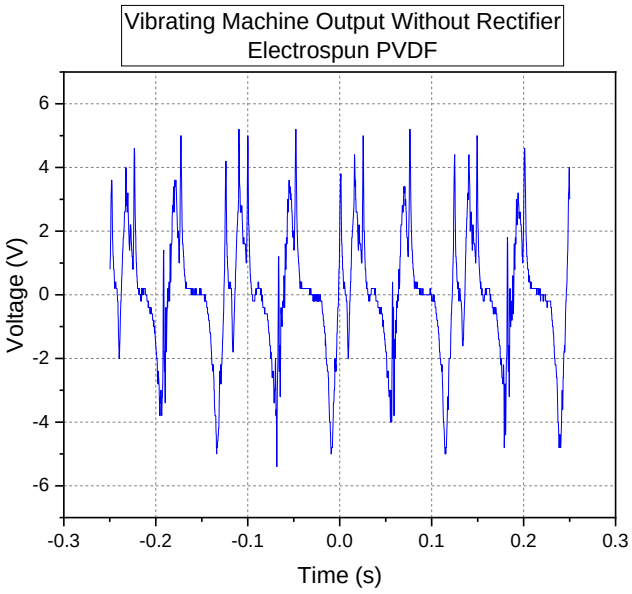

Figure 51: Electrospun PVDF energy harvester response before the rectifier

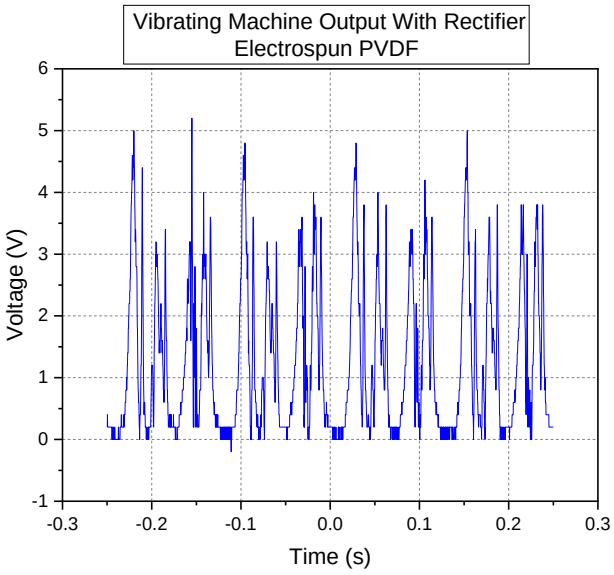

Figure 52: Electrospun PVDF energy harvester response after the rectifier

A 1000µF capacitor was charged using this energy harvester. Figure 53 shows the capacitor charging over time. The capacitor charges around 34 mV every 30 seconds for the electrospun PVDF nanofiber mat.

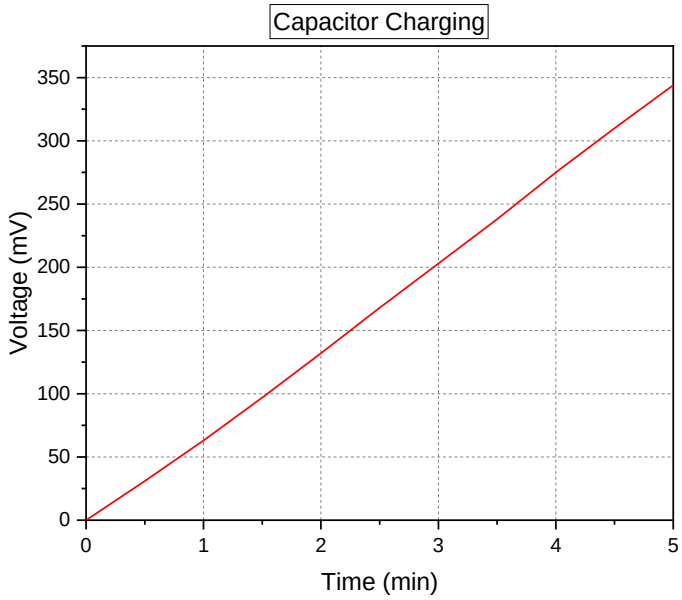

Figure 53: Capacitor charging due to the electrospun PVDF energy harvester

CHAPTER V

SUMMARY AND FUTURE WORK

In electrospun samples, β-phase has clearly increased compared to the PVDF bulk material. Electrospun PVDF shows a very high β phase. It can be seen in Table 2, the combined β and γ phase percentage in electrospun PVDF is 89.49% while the β phase is 75.7%. The voltage response for electrospun PVDF 41 V which is the highest of all the nanofibers that were tested. Contrary to the literature review, addition of MWCNTs and BTO did not improve the β-phase in electrospun PVDF.

β-phase in forcespun PVDF is quite low compared to electrospun PVDF. Although, the time required for fabrication of PVDF nanofibers using forcespinning is much lower than that with electrospinning. Addition of MWCNTs and BTO was able to increase the β-phase in forcespun PVDF nanofibers. PVDF/MWCNTs showed best voltage response of 37 V.

As explained in Section I, stretching PVDF induces β phase. During nanofiber fabrication in electrospinning, the fibers are stretched due to high electric voltage and rotating collector. During forcespinning, the fibers are stretched due to the centrifugal forces. Thus, these processes induce β phase in PVDF. As seen in SEM analysis, fibers with forscespinning show lumps of PVDF while electrospinning shows none. This indicates that in forcespinning, the fibers are not stretched enough thus affecting the occurrence of β phase in PVDF nanofibers.

The high voltage response indicated that these nanofibers will also be good candidates for sensing applications. PVDF being a biocompatible polymer, PVDF nanofibers are good candidates for biomedical sensors as well.

For energy harvesting testing, were able to successfully charge a 1000 μF capacitor using a vibrating machine and PVDF nanofibers. This indicates that the nanofiber mat cantilever can be used for energy harvesting applications where it will harness the energy vibrations in the environment.

5.1 Future Work

For improving the piezoelectric response, the nanofiber mats should be poled. Poling is the process of applying a high the electric voltage across a piezoelectric fiber mat. The high electric voltage aligns the dipoles in the fibers thus increasing the piezoelectric response and increasing the β-phase.

Next step will be implementing the energy harvester for a practical application. This energy harvester can be used in powering micro-electronics in remote areas. Another application will be as a sensor in biomedical applications and self-powered structure monitoring sensor.

REFERENCES

Abdalla, S., Obaid, A., & Al-Marzouki, F. M. (2016). Preparation and characterization of poly (vinylidene fluoride): A high dielectric performance nanocomposite for electrical storage. Results in physics, 6, 617-626.

Acosta, M., Novak, N., Rojas, V., Patel, S., Vaish, R., Koruza, J., ... & Rödel, J. (2017). $BaTiO_3$-based piezoelectrics: Fundamentals, current status, and perspectives. Applied Physics Reviews, 4(4), 041305.

Akin Yildirim, Y., Toprak, A., & Tigli, O. (2018). Piezoelectric Membrane Actuators for Micropump Applications Using PVDF-TrFE. Journal of Microelectromechanical Systems, 27(1), 86-94.

Anton, S., & Sodano, H. (2007). A review of power harvesting using piezoelectric materials. Smart materials and structutres, 16(3),

Ballato, A. (1995). Piezoelectricity: old effect, new thrusts. IEEE transactions on ultrasonics, ferroelectrics, and frequency control, 42(5), 916-926.

Briscoe, J., & Dunn, S. (2015). Piezoelectric nanogenerators–a review of nanostructured piezoelectric energy harvesters. Nano Energy, 14, 15-29.

Broadhurst, M. G., & Davis, G. T. (1984). Physical basis for piezoelectricity in PVDF. Ferroelectrics, 60(1), 3-13.

Cadek, M., Coleman, J. N., Ryan, K. P., Nicolosi, V., Bister, G., Fonseca, A., Nagy, J. B., Szostak, K., Beguin, F., & Blau, W. J. (2004). Reinforcement of polymers with carbon nanotubes: the role of nanotube surface area. Nano letters, 4(2), 353-356.

Cai, X., Lei, T., Sun, D., & Lin, L. (2017). A critical analysis of the α, β and γ phases in poly (vinylidene fluoride) using FTIR. RSC advances, 7(25), 15382-15389.

Castkova, K., Kastyl, J., Sobola, D., Petrus, J., Stastna, E., Riha, D., & Tofel, P. (2020). Structure–Properties Relationship of Electrospun PVDF Fibers. Nanomaterials, 10(6), 1221.

Chung, S. Y., Kim, S., Lee, J. H., Kim, K., Kim, S. W., Kang, C. Y., ... & Kim, Y. S. (2012). All-solution-processed flexible thin film piezoelectric nanogenerator. Advanced Materials, 24(45), 6022-6027.

Elahi, H., Eugeni, M., & Gaudenzi, P. (2018). A review on mechanisms for piezoelectric-based energy harvesters. Energies, 11(7), 1850.

Eom, J., Lee, J., Lee, H., & Choi, B. (2013, October). Energy harvesting for bladder pressure sensor using parametric amplification phenomenon of PVDF bimorph cantilever. In The 6th 2013 Biomedical Engineering International Conference (pp. 1-3). IEEE.

Fu, Y., Harvey, E. C., Ghantasala, M. K., & Spinks, G. M. (2005). Design, fabrication and testing of piezoelectric polymer PVDF microactuators. Smart materials and structures, 15(1), S141.

Fukada, E. (1968). Piezoelectricity as a fundamental property of wood. Wood Science and Technology, 2(4), 299-307.

Fukada, E. (2000). History and recent progress in piezoelectric polymers. IEEE Transactions on ultrasonics, ferroelectrics, and frequency control, 47(6), 1277-1290.

Hwang, G. T., Park, H., Lee, J. H., Oh, S., Park, K. I., Byun, M., ... & Lee, K. J. (2014). Self-powered cardiac pacemaker enabled by flexible single crystalline PMN-PT piezoelectric energy harvester. Advanced materials, 26(28), 4880-4887.

Horrocks, A. R., & Anand, S. C. (Eds.). (2000). Handbook of technical textiles. Elsevier.

Inkson, B. J. (2016). Scanning electron microscopy (SEM) and transmission electron microscopy (TEM) for materials characterization. In Materials characterization using nondestructive evaluation (NDE) methods (pp. 17-43). Woodhead Publishing.

Jin, L., Ma, S., Deng, W., Yan, C., Yang, T., Chu, X., ... & Yang, W. (2018). Polarization-free high-crystallization β-PVDF piezoelectric nanogenerator toward self-powered 3D acceleration sensor. Nano Energy, 50, 632-638.

Jiyong, H., Yinda, Z., Hele, Z., Yuanyuan, G., & Xudong, Y. (2017). Mixed effect of main electrospinning parameters on the β-phase crystallinity of electrospun PVDF nanofibers. Smart Materials and Structures, 26(8), 085019

Jung, J. H., Lee, M., Hong, J. I., Ding, Y., Chen, C. Y., Chou, L. J., & Wang, Z. L. (2011). Lead-free NaNbO3 nanowires for a high output piezoelectric nanogenerator. ACS nano, 5(12), 10041-10046.

Kaczmarek, H., Królikowski, B., Klimiec, E., Chylińska, M., & Bajer, D. (2019). Advances in the study of piezoelectric polymers. Russian Chemical Reviews, 88(7), 749

Kawai, H. (1969). The piezoelectricity of poly (vinylidene fluoride). Japanese journal of applied physics, 8(7), 975.

Kim, G. H., Hong, S. M., & Seo, Y. (2009). Piezoelectric properties of poly (vinylidene fluoride) and carbon nanotube blends: β-phase development. Physical chemistry chemical physics, 11(44), 10506-10512.

Koç, M., Paralı, L., & Şan, O. (2020). Fabrication and vibrational energy harvesting characterization of flexible piezoelectric nanogenerator (PEN) based on PVDF/PZT. Polymer Testing, 90, 106695.

Li, L., Zhang, M., Rong, M., & Ruan, W. (2014). Studies on the transformation process of PVDF from α to β phase by stretching. RSC Advances, 4(8), 3938-3943.

Liu, Z. H., Pan, C. T., Lin, L. W., & Lai, H. W. (2013). Piezoelectric properties of PVDF/MWCNT nanofiber using near-field electrospinning. Sensors and Actuators A: Physical, 193, 13-24.

Liu, Z., Zhang, S., Jin, Y. M., Ouyang, H., Zou, Y., Wang, X. X., ... & Li, Z. (2017). Flexible piezoelectric nanogenerator in wearable self-powered active sensor for respiration and healthcare monitoring. Semiconductor Science and Technology, 32(6), 064004.

Lu, M. P., Song, J., Lu, M. Y., Chen, M. T., Gao, Y., Chen, L. J., & Wang, Z. L. (2009). Piezoelectric nanogenerator using p-type ZnO nanowire arrays. Nano letters, 9(3), 1223-1227.

Mahadeva, S. K., Berring, J., Walus, K., & Stoeber, B. (2013). Effect of poling time and grid voltage on phase transition and piezoelectricity of poly (vinyledene fluoride) thin films using corona poling. Journal of physics D: applied physics, 46(28), 285305.

Mahanty, B., Maity, K., Sarkar, S., & Mandal, D. (2020). Human skin interactive self-powered piezoelectric e-skin based on PVDF/MWCNT electrospun nanofibers for non-invasive health care monitoring. Materials Today: Proceedings, 21, 1964-1968.

Maiti, S., Karan, S. K., Lee, J., Mishra, A. K., Khatua, B. B., & Kim, J. K. (2017). Bio-waste onion skin as an innovative nature-driven piezoelectric material with high energy conversion efficiency. Nano Energy, 42, 282-293.

Martins, P., Lopes, A. C., & Lanceros-Mendez, S. (2014). Electroactive phases of poly (vinylidene fluoride): Determination, processing and applications. Progress in polymer science, 39(4), 683-706.

Mohamed, M. A., Jaafar, J., Ismail, A. F., Othman, M. H. D., & Rahman, M. A. (2017). Fourier transform infrared (FTIR) spectroscopy. In Membrane Characterization (pp. 3-29). Elsevier.

Mokhtari, F., Latifi, M., & Shamshirsaz, M. (2015). Electrospinning/electrospray of polyvinylidene fluoride (PVDF): piezoelectric nanofibers. The Journal of The Textile Institute, 1-19.

Mokhtari, F., Latifi, M., & Shamshirsaz, M. (2016). Electrospinning/electrospray of polyvinylidene fluoride (PVDF): piezoelectric nanofibers. The Journal of The Textile Institute, 107(8), 1037-1055.

More, N., & Kapusetti, G. (2017). Piezoelectric material–a promising approach for bone and cartilage regeneration. Medical hypotheses, 108, 10-16.

Motamedi, A. S., Mirzadeh, H., Hajiesmaeilbaigi, F., Bagheri-Khoulenjani, S., & Shokrgozar, M. (2017). Effect of electrospinning parameters on morphological properties of PVDF nanofibrous scaffolds. Progress in biomaterials, 6(3), 113-123.

Mould, R. F. (2007). Pierre Curie, 1859–1906. Current oncology, 14(2), 74.

Nishiyama, T., Sumihara, T., Sasaki, Y., Sato, E., Yamato, M., & Horibe, H. (2016). Crystalline structure control of poly(vinylidene fluoride) films with the antisolvent addition method. Polymer Journal, 48(10), 1035-1038.

Park, S., Kim, Y., Jung, H., Park, J. Y., Lee, N., & Seo, Y. (2017). Energy harvesting efficiency of piezoelectric polymer film with graphene and metal electrodes. Scientific reports, 7(1), 1-8.

Popov, V. N. (2004). Carbon nanotubes: properties and application. Materials Science and Engineering: R: Reports, 43(3), 61-102.

Pavlović, V. P., Pavlović, V. B., Vlahović, B., Božanić, D. K., Pajović, J. D., Dojčilović, R., & Djoković, V. (2013). Structural properties of composites of polyvinylidene fluoride and mechanically activated BaTiO3 particles. Physica Scripta, 2013(T157), 014006.

Ribeiro, C., Sencadas, V., Ribelles, J. L. G., & Lanceros-Méndez, S. (2010). Influence of processing conditions on polymorphism and nanofiber morphology of electroactive poly (vinylidene fluoride) electrospun membranes. Soft Materials, 8(3), 274-287.

Safaei, M., Sodano, H. A., & Anton, S. R. (2019). A review of energy harvesting using piezoelectric materials: state-of-the-art a decade later (2008–2018). Smart Materials and Structures, 28(11), 113001.

Saha, S., Yauvana, V., Chakraborty, S., & Sanyal, D. (2019). Synthesis and Characterization of Polyvinylidene-fluoride (PVDF) Nanofiber for Application as Piezoelectric Force Sensor. Materials Today: Proceedings, 18(3), 1450-1458.

Sarkar, K., Gomez, C., Zambrano, S., Ramirez, M., de Hoyos, E., Vasquez, H., & Lozano, K. (2010). Electrospinning to forcespinning™. Materials today, 13(11), 12-14.

Sathya, P. (2020, February). Bimorph Piezoelectric Energy Harvester at Low Frequency. In 2020 International Conference on Emerging Trends in Information Technology and Engineering (ic-ETITE) (pp. 1-5). IEEE.

Sencadas, V., Gregorio Jr, R., & Lanceros-Méndez, S. (2009). α to β phase transformation and microestructural changes of PVDF films induced by uniaxial stretch. Journal of Macromolecular Science®, 48(3), 514-525.

Seol, M. L., Choi, J. M., Kim, J. Y., Ahn, J. H., Moon, D. I., & Choi, Y. K. (2013). Piezoelectric nanogenerator with a nanoforest structure. Nano Energy, 2(6), 1142-1148.

Sharafkhani, S., & Kokabi, M. (2020). Ultrathin-shell PVDF/CNT nanocomposite aligned hollow fibers as a sensor/actuator single element. Composites Science and Technology, 200, 108425.

Shuai, C., Liu, G., Yang, Y., Yang, W., He, C., Wang, G., ... & Peng, S. (2020). Functionalized BaTiO3 enhances piezoelectric effect towards cell response of bone scaffold. Colloids and Surfaces B: Biointerfaces, 185, 110587.

Singh, P. K., Gaur, M. S., Johari, D., Sagar, R., Gupta, A., Sharma, A., ... & Yadav, M. (2019). Enhanced pyroelectric and piezoelectric properties of PVDF–BaTiO3 nanocomposites layered samples. Ferroelectrics, 551(1), 122-132.

Sirohi, J., & Chopra, I. (2000). Fundamental understanding of piezoelectric strain sensors. Journal of intelligent material systems and structures, 11(4), 246-257.

Stanjek, H., & Häusler, W. J. H. I. (2004). Basics of X-ray Diffraction. Hyperfine interactions, 154(1), 107-119

Swallow, L. M., Luo, J. K., Siores, E., Patel, I., & Dodds, D. (2008). A piezoelectric fibre composite based energy harvesting device for potential wearable applications. Smart Materials and Structures, 17(2), 025017.

Ting, Y., Gunawan, H., Sugondo, A., & Chiu, C. W. (2013). A new approach of polyvinylidene fluoride (PVDF) poling method for higher electric response. Ferroelectrics, 446(1), 28-38.

Tiwari, V., & Srivastava, G. (2014). Effect of thermal processing conditions on the structure and dielectric properties of PVDF films. Journal of Polymer Research, 21(11), 1-8.

Vijaya, M.S. (2013). Piezoelectric Materials and Devices: Applications in Engineering and Medical Sciences. CRC Press, Boca Raton.

Vernon-Parry, K. D. (2000). Scanning electron microscopy: an introduction. III-Vs Review, 13(4), 40-44.

Wang, X. (2012). Piezoelectric nanogenerators—Harvesting ambient mechanical energy at the nanometer scale. Nano Energy, 1(1), 13-24.

Wang, X., Sun, F., Yin, G., Wang, Y., Liu, B., & Dong, M. (2018). Tactile-Sensing Based on Flexible PVDF Nanofibers via Electrospinning: A Review. Sensors, 18(2), 330

Wang, Z. L., & Song, J. (2006). Piezoelectric nanogenerators based on zinc oxide nanowire arrays. Science, 312(5771), 242-246.

Wu, H., Tang, L., Yang, Y., & Soh, C. K. (2013). A novel two-degrees-of-freedom piezoelectric energy harvester. Journal of Intelligent Material Systems and Structures, 24(3), 357-368.

Xiong, H., & Wang, L. (2016). Piezoelectric energy harvester for public roadway: On-site installation and evaluation. Applied Energy, 174, 101-107.

Yang, X., Wang, Y., & Qing, X. (2019). A flexible capacitive sensor based on the electrospun PVDF nanofiber membrane with carbon nanotubes. Sensors and Actuators A: Physical, 299, 111579.

Yang, Y., Pan, H., Xie, G., Jiang, Y., Chen, C., Su, Y., ... & Tai, H. (2020). Flexible piezoelectric pressure sensor based on polydopamine-modified BaTiO3/PVDF composite film for human motion monitoring. Sensors and Actuators A: Physical, 301, 111789.

Yu, L., Zhou, P., Wu, D., Wang, L., Lin, L., & Sun, D. (2019). Shoepad nanogenerator based on electrospun PVDF nanofibers. Microsystem Technologies, 25(8), 3151-3156.

Zhao, Y., Liao, Q., Zhang, G., Zhang, Z., Liang, Q., Liao, X., & Zhang, Y. (2015). High output piezoelectric nanocomposite generators composed of oriented BaTiO3 NPs@ PVDF. Nano Energy, 11, 719-727.

APPENDIX

APPENDIX

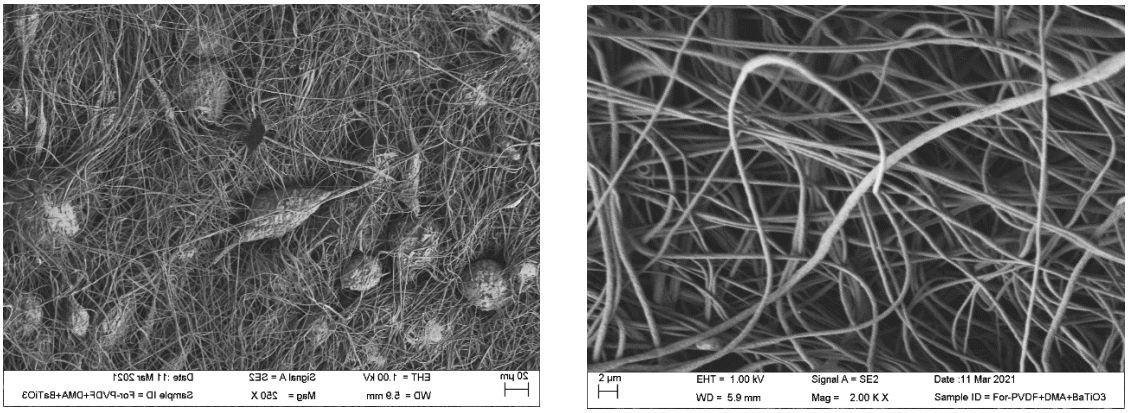

(a)

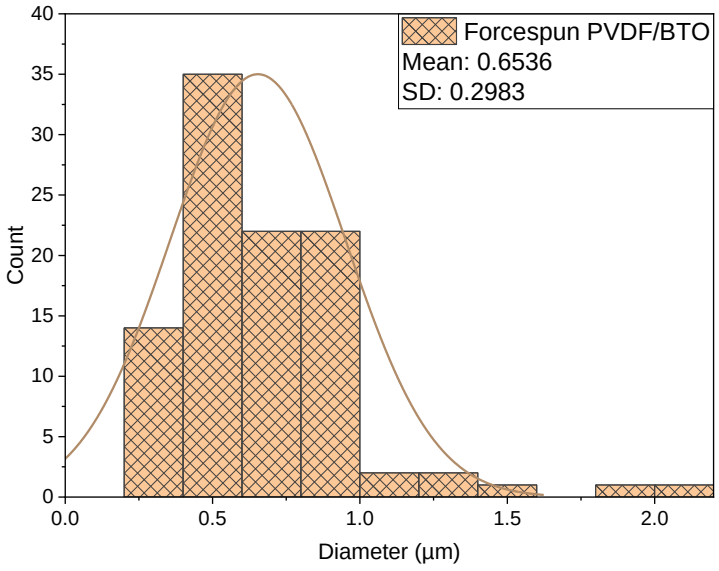

(b)

Figure 54: (a) SEM Images of forcespun PVDF/BTO nanofibers and (b) diameter distribution on forcespun PVDF/BTO nanofibers.

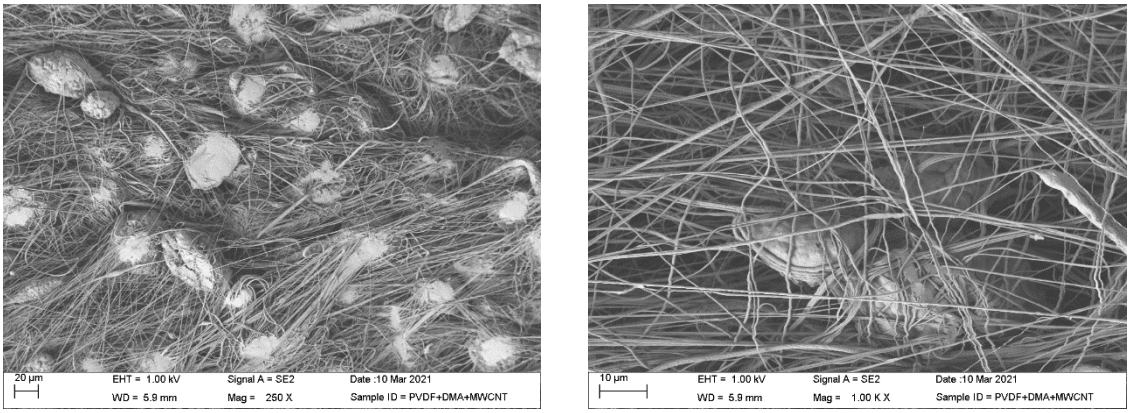

(a)

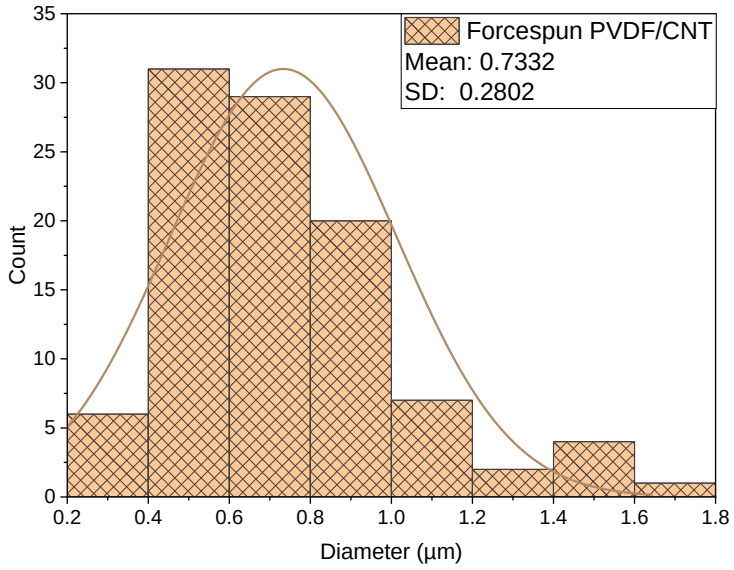

(b)

Figure 55: (a) SEM Images of forcespun PVDF/MWCNT nanofibers and (b) diameter distribution on forcespun PVDF/MWCNT nanofibers.

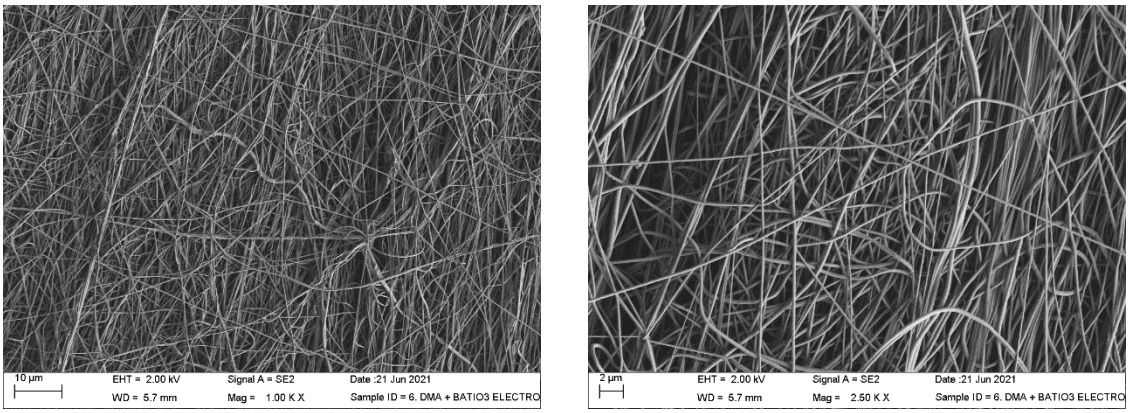

(a)

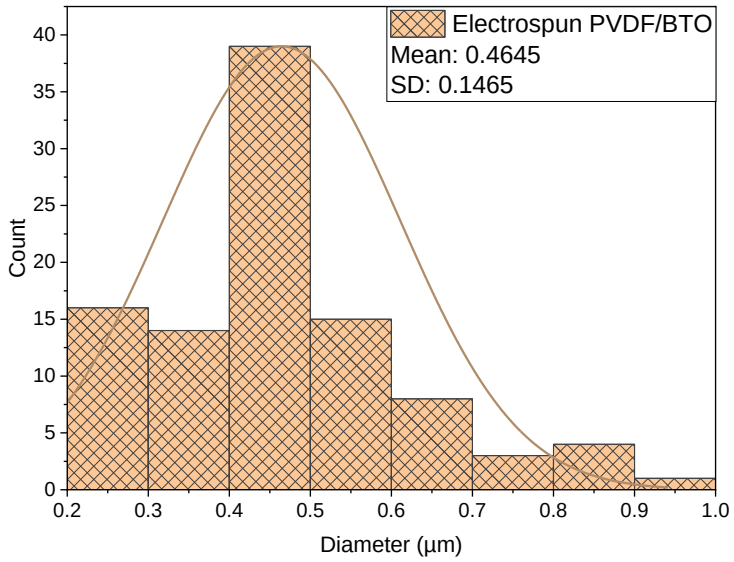

(b)

Figure 56: (a) SEM Images of electrospun PVDF/BTO nanofibers and (b) diameter distribution on electrospun PVDF/BTO nanofibers.

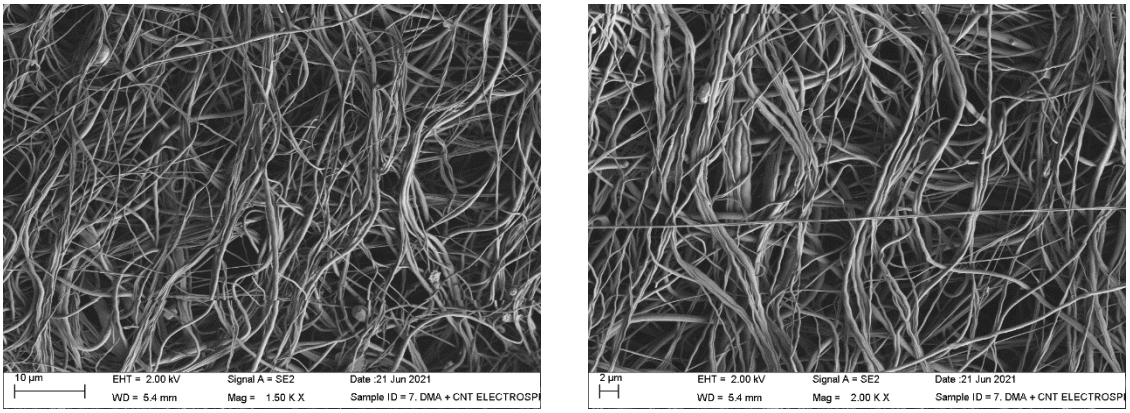

(a)

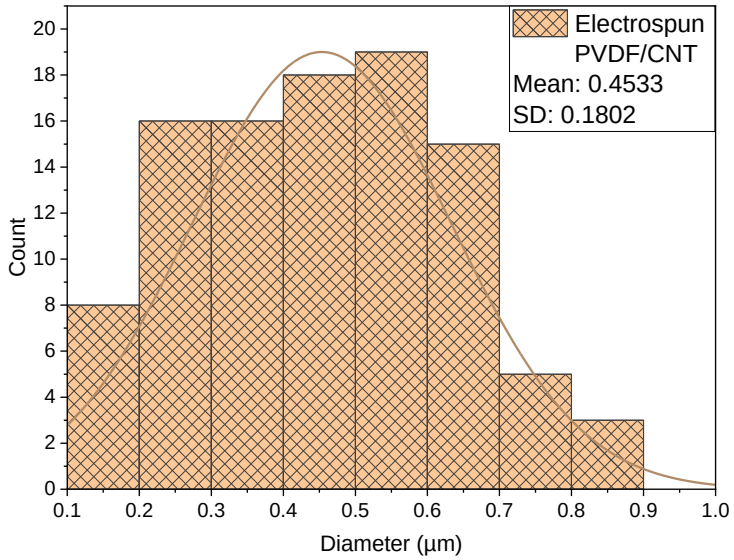

(b)

Figure 57: (a) SEM Images of electrospun PVDF/MWCNT nanofibers and (b) diameter distribution on electrosspun PVDF/MWCNT nanofibers.

BIOGRAPHICAL SKETCH

Jui Vitthal Kharade pursued her bachelor's degree in mechanical engineering in June 2019 from Savitribai Phule Pune University in India. She earned her Master of Science degree in mechanical engineering from University of Texas Rio Grande Valley in August 2021. During her master's, she worked as a research assistant and as a teaching assistant.

Email Address: Juikharade@gmail.com.